minerals

Article

Zones of PGE–Chromite Mineralization in Relation to Crystallization of the Pados-Tundra Ultramafic Complex, Serpentinite Belt, Kola Peninsula, Russia

Andrei Y. Barkov [1,*], **Andrey A. Nikiforov** [1], **Larisa P. Barkova** [1], **Vladimir N. Korolyuk** [2] and **Robert F. Martin** [3]

[1] Research Laboratory of Industrial and Ore Mineralogy, Cherepovets State University, 5 Lunacharsky Avenue, 162600 Cherepovets, Russia; ultramafic-rock@mail.ru (A.A.N.); larisa-p-barkova@mail.ru (L.P.B.)

[2] V.S. Sobolev Institute of Geology and Mineralogy, Siberian Branch of the Russian Academy of Science, 3 Avenue "Prospekt Koptyuga", 630090 Novosibirsk, Russia; camebax@igm.nsc.ru

[3] Department of Earth and Planetary Sciences, McGill University, 3450 University Street, Montreal, QC H3A 0E8, Canada; robert.martin@mcgill.ca

[*] Correspondence: ore-minerals@mail.ru; Tel.: +7-(8202)-55-65-97

Abstract: The lopolithic Pados-Tundra layered complex, the largest member of the Serpentinite belt–Tulppio belt (SB–TB) megastructure in the Fennoscandian Shield, is characterized by (1) highly magnesian compositions of comagmatic dunite–harzburgite–orthopyroxenite, with primitive levels of high-field-strength elements; (2) maximum values of Mg# in olivine (Ol, 93.3) and chromian spinel (Chr, 57.0) in the Dunite block (DB), which exceed those in Ol (91.7) and Chr (42.5) in the sills at Chapesvara, and (3) the presence of major contact-style chromite–IPGE-enriched zones hosted by the DB. A single batch of primitive, Al-undepleted komatiitic magma crystallized normally as dunite close to the outer contact, then toward the center. A similar magma gave rise to Chapesvara and other suites of the SB–TB megastructure. Crystallization proceeded from the early Ol + Chr cumulates to the later Ol–Opx and Opx cumulates with accessory Chr in the Orthopyroxenite zone. The accumulation of Chr resulted from efficient cooling along boundaries of the Dunite block. The inferred front of crystallization advanced along a path traced by vectors of Ol and Chr compositions. Grains and aggregates of Chr were mainly deposited early after the massive crystallization of olivine. Chromium, Al, Zn and H_2O, all incompatible in Ol, accumulated to produce podiform segregations or veins of chromitites. This occurred episodically along the moving front of crystallization. Crystallization occurred rapidly owing to heat loss at the contact and to a shallow level of emplacement. The Chr layers are not continuous but rather heterogeneously distributed pods or veins of Chr–Ol–clinochlore segregations. Isolated portions of melt enriched in H_2O and ore constituents accumulated during crystallization of Ol. Levels of fO_2 in the melt and, consequently, the content of ferric iron in Chr, increased progressively, as in other intrusions of the SB–TB megastructure. The komatiitic magma vesiculated intensely, which led to a progressive loss of H_2 and buildup in fO_2. In turn, this led to the appearance of anomalous Chr–Ilm parageneses. Diffuse rims of Chr grains, abundant in the DB, contain elevated levels of Fe^{3+} and enrichments in Ni and Mn. In contrast, Zn is preferentially partitioned into the core, leading to a decoupling of Zn from Mn, also known at Chapesvara. The sulfide species display a pronounced Ni-(Co) enrichment in assemblages of cobaltiferous pentlandite, millerite (and heazlewoodite at Khanlauta), deposited at ≤630 °C. The oxidizing conditions have promoted the formation of sulfoselenide phases of Ru in the chromitites. The attainment of high degrees of oxidation during crystallization of a primitive parental komatiitic magma accounts for the key characteristics of Pados-Tundra and related suites of the SB–TB megastructure.

Keywords: chromite mineralization; ultramafic complexes; hypabyssal intrusions; highly magnesian magma; komatiites; oxidation; Pados-Tundra complex; Serpentinite Belt; Kola Peninsula; Fennoscandian Shield; Russia

1. Introduction

Occurrences of chromite mineralization are intimately associated with complexes of ultramafic rocks emplaced in various tectonic settings, especially with ophiolites, Ural-ian–Alaskan-type complexes and lower units of layered intrusions, or with placers derived from such complexes [1–6]. Chromitite zones are important because they are the well-recognized source not only of Cr (plus accompanying Fe, Ti and V), but also of platinum-group elements (PGE) of the iridium subgroup: Os, Ir and Ru, or IPGE [7,8]. In addition, chromitites are a useful monitor of mantle processes, petrogenesis, conditions of magmatic fractionation and variations in levels of oxygen fugacity (fO$_2$) during the crystallization of magmatic complexes [9–12].

We provide new results on the mineralogy, geochemistry and petrogenesis of the large Pados-Tundra complex and its Cr mineralization. Pados-Tundra is the largest member of the Serpentinite belt of subvolcanic bodies. The overall extent of this belt, which consists of numerous bodies of fairly fresh to entirely serpentinized, variously foliated and altered ultramafic rocks, exceeds 200 km along a curved boundary to the southwestern end of the Sal'nie Tundry area in the Kola Peninsula [13–15] in the Fennoscandian Shield (Figure 1).

Our previous investigations revealed the existence of cryptic layering, the development of an unconventional type of PGE mineralization, and uncommon forms of spheroidal weathering in the Pados-Tundra complex [16–18]. In the Chapesvara and Lyavaraka complexes of the Serpentinite belt, we reported on anomalous parageneses of chromite–ilmenite mineralization [19]. We inferred the existence of shallow plutonic associations in the Pados-Tundra and Malyi Pados complexes and in the zoned Chapesvara sills. These presumably all crystallized comagmatically from a primitive, Al-undepleted and highly magnesian komatiitic magma [20]. The process of double-front crystallization documented at Chapesvara represents the first example reported in a highly magnesian subvolcanic complex [20]. A Paleoproterozoic age is indicated for the Pados-Tundra complex on the basis of the Sm–Nd and U–Pb isotopic systems [21]. Our objectives here are to further characterize the Pados-Tundra complex texturally and mineralogically, and to build on comparisons with the closely associated comagmatic suites at Chapesvara [19,20] and Khanlauta [22].

Geological Background

The Serpentinite belt consists of several suites and fragmented bodies; in addition to Pados-Tundra, these include the large sills at Chapesvara (I and II), Lotmvara (I and II), the flows at Khanlauta, along with the Kareka-Tundra and Termo-Tundra suites. On a regional scale, the belt extends over 30 km. These suites of subvolcanic origin are clustered near the Russian–Finnish border, and are traced further in a northeasterly direction, and also to the west, to form the Tulppio belt in Finland [23]. These suites are members of a transregional megastructure, the "Serpentinite belt—Tulppio belt" or SB–TB structure [22], an important component of the Fennoscandian Shield. This structure has a Paleoproterozoic age, as indicated by results of Sm–Nd dating of the Pados-Tundra complex: 2485 ± 38 Ma [21].

The ultramafic intrusions making up the Serpentinite belt are closely associated with major shear zones accompanied by a collisional mélange developed as a part of the Tanaelv high-grade ductile thrust belt (Figure 1). They are positioned along the curved boundary of the two large terranes of the Baltic Shield: the Paleoproterozoic Lapland Granulite Terrane, LGT (or Lapland Granulite Belt), forming part of the Paleoproterozoic Lapland–Kola Collisional Orogen (LKCO), and the Belomorian Composite Terrane (BCT) of Archean age [24]. These sill-like bodies formed by injection of a primitive komatiitic magma, derived from a common mantle source, along a subparallel system of northeast-trending regional shear zones [20].
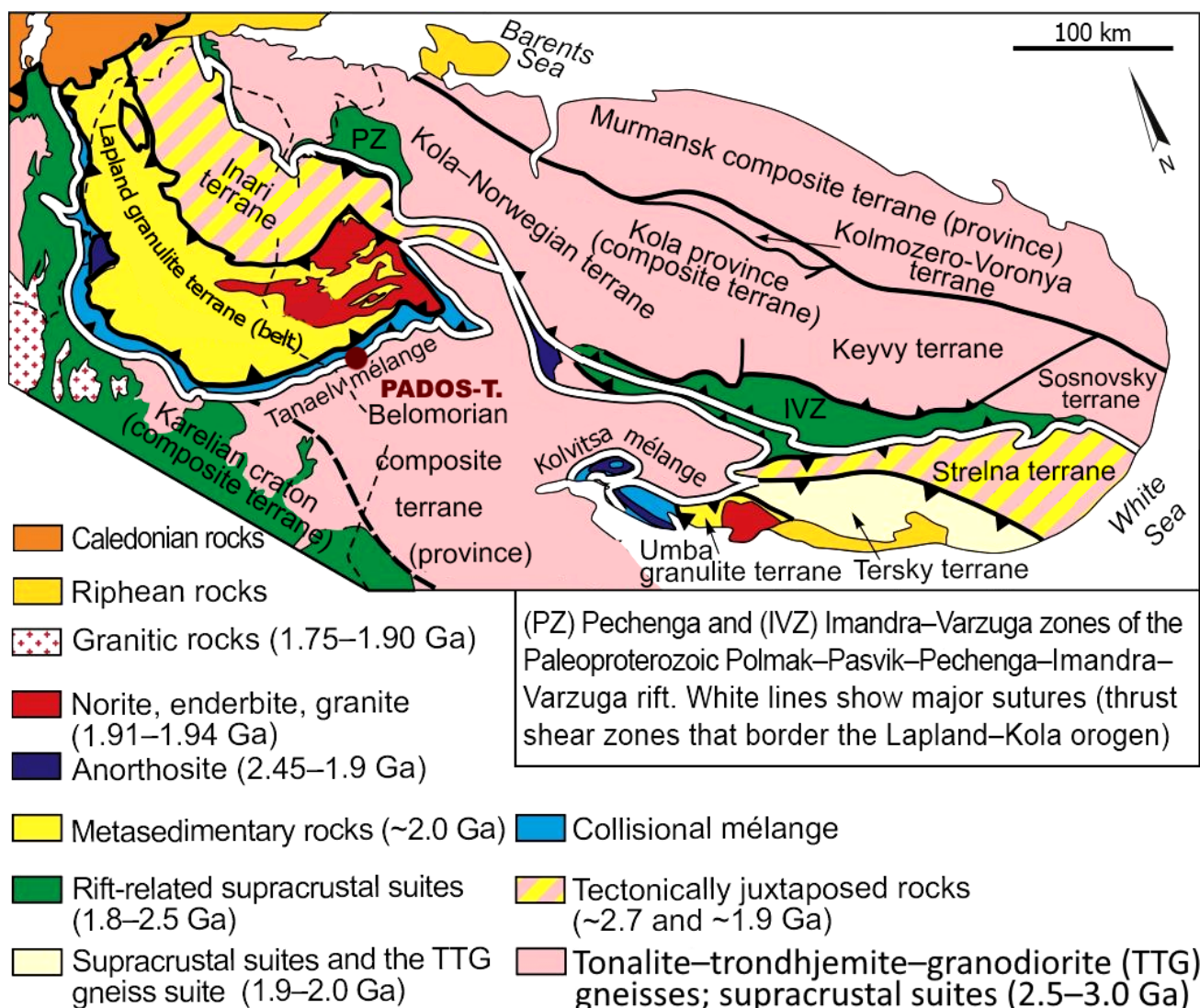
Figure 1. Location of the Pados-Tundra complex shown in the context of tectonic settings in the northeastern part of the Fennoscandian Shield (after [24] and references therein).

According to [16], the Pados-Tundra complex has a lopolith-like structure formed by the lower Dunite and Orthopyroxenite zones. The chromite occurrences display a stratiform arrangement of three major layers (Figure 2a) composed of chromitite pods and veins, which are hosted by the Dunite block [15]. The results of our latest investigations indicate that in the Pados-Tundra body, one finds the same sequence of dunite—harzburgite—orthopyroxenite rocks as in the Chapesvara and Malyi Pados suites. The latter (Figure 2b) is no longer proposed to be a tectonically dislocated fragment of Pados-Tundra, but is instead another large representative of the belt produced from the komatiitic source and comagmatic with Pados-Tundra. In addition, we interpret the contact rocks of gabbroic affinity, i.e., gabbro or chlorite–mica–amphibole rock mapped by previous investigators (Figure 2a,b), to represent hybrid rocks contaminated by wallrocks.
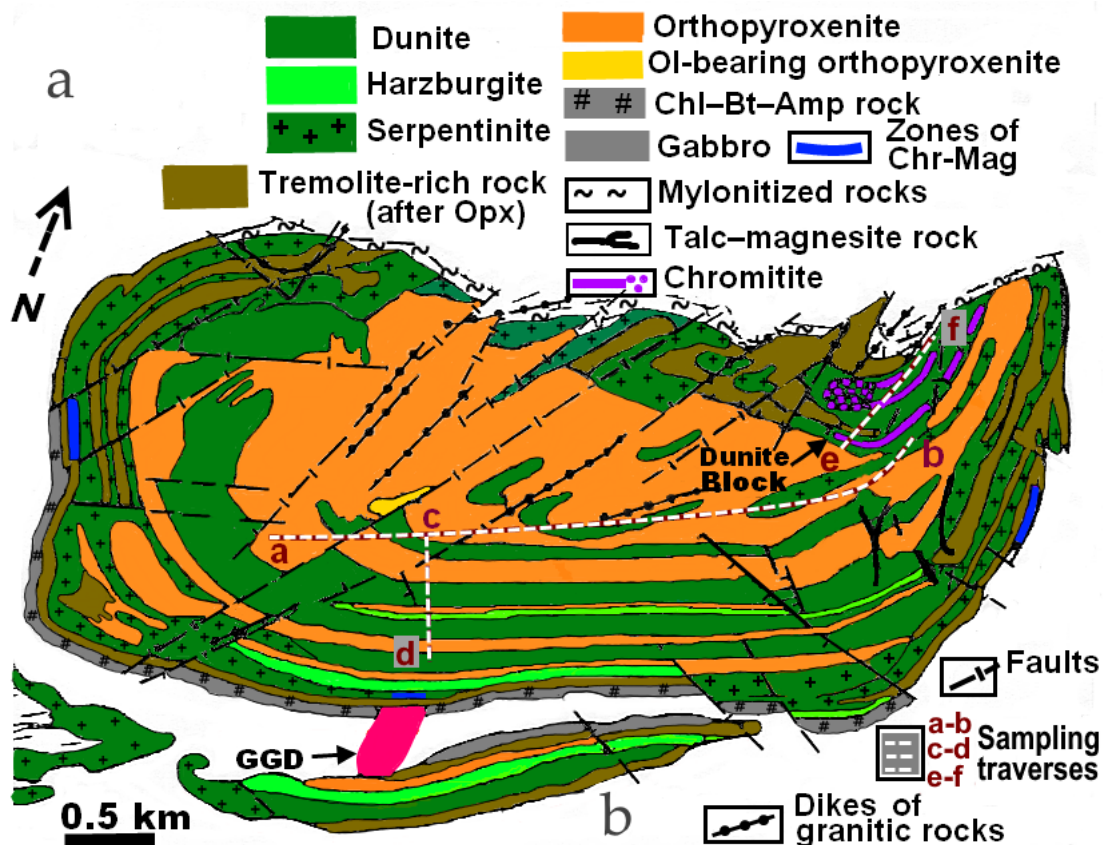
Figure 2. Geological map of the Pados-Tundra complex (**a**), and of the associated Malyi Pados massif (**b**), modified from [15]. The lines *a–b*, *c–d* and *e–f* display the sampling traverses involved in the present investigation. Stratiform layers, segregations and orebodies of chromitite are shown schematically in purple; these zones mineralized in chromian spinel (Chr) are hosted by the Dunite block. In addition, zones of mineralization enriched in Chr are present at the outer contact; these are shown in blue. GGD: granite–gneiss dome.

2. Materials and Methods

Our materials consist of about four hundred samples of rocks and polished mounts of ore-bearing assemblages bearing chromian spinel (Chr), mostly sampled along the profiles *a–b*, *c–d*, and *e–f* (Figure 3a,b). The profile *e–f* extends across the major zones of chromitite ores hosted by the Dunite block, and is oriented toward and close to the outer contact. It is not a single line *sensu stricto*, but is combined from results of two subparallel routes within 0.1 km of the line. Such an approach ensures a better representation of the podiform chromitites. Point locations of samples collected along the two routes were then projected onto the *e–f* line for the sake of clarity of interpretations (Figure 3b).

Our interpretations are based on results of a total of about two thousand data-points analyzed quantitatively by wavelength-dispersive spectroscopy (WDS) and electron-probe microanalysis. In addition, we used original data obtained for the Mount Khanlauta suite located about 2 km southwest of Pados-Tundra (Figure 3a). According to the findings reported in [22], this suite is a differentiated flow composed of two zones of harzburgite (~0.15 km thick) crystallized from a komatiitic magma; in one of the outcrops, it exhibits columnar jointing, yielding hexagonal cross-sections. Relevant comparisons are also made with neighboring suites, i.e., with zoned sills of the Chapesvara suite [20] located about 8 km northeast of Pados-Tundra.
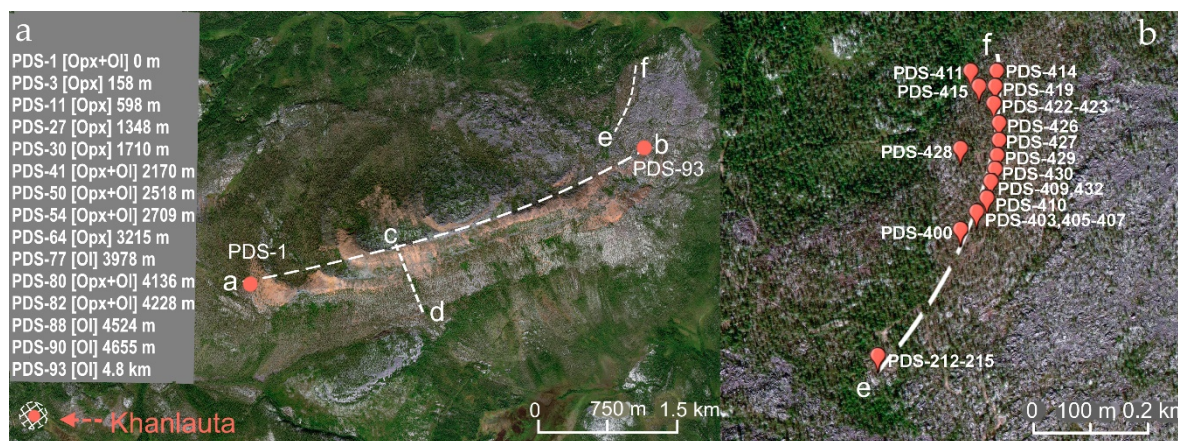
Figure 3. (**a**) Location of the major profiles of sampling (*a–b*, *c–d* and *e–f*) across the Pados-Tundra layered complex, as shown on a SAS.Planet image. The inset shows typical examples of overlying associations composed of orthopyroxene (Opx), olivine (Ol) and Opx–Ol cumulates along the longest traverse *a–b*. Relative distances (in meters) are shown in the order from the sample PDS-1 to #93. The profile *c–d* also reveals the overlying sequences of Opx and Opx–Ol cumulates, represented by the analyzed samples PDS-105 to #111. The *e–f* profile (**b**) is oriented toward the outer contact and across the major zones of chromite mineralization hosted by the Dunite block (samples PDS-212-215 to 400-432). The location of the Khanlauta suite also is shown (**a**), about 2 km southwest of Pados-Tundra. The other neighboring suites are the zoned sills at Chapesvara [20], located at a distance of about 8 km northeast of Pados-Tundra.

Whole-rock major- and trace-element analyses were performed in the Analytical Center for multi-elemental and isotope studies, SB RAS, Novosibirsk, Russia. Contents of major and minor elements were established via X-ray fluorescence analysis (XRF) using the facility ARL-9900XP (Thermo Fisher Scientific Ltd., Waltham, MA, USA). Levels of high-field-strength elements (HFSE), including the rare-earth elements (REE), were measured by high-resolution inductively coupled plasma—mass spectrometry (ICP–MS) using the instrument ELEMENT (Finnigan MAT, San Jose, CA, USA). Analytical details have been described [25–27]. Reliance on the same sets of facilities and analytical conditions used to characterize the three suites was deemed essential to avoid potential discrepancies due to technical differences.

The minerals were analyzed using a JEOL JXA-8100 instrument (JEOL Ltd., Tokyo, Japan) operated in the WDS mode. An accelerating voltage of 20 kV and a probe current of 50 nA were used. We employed $K\alpha$ analytical lines for all elements except for Cr; the $K\beta_1$ line was used because of peak overlap. Periods of measurements at the peaks were 20 or 10 s. The superposition of the Ti$K\beta_1$ line on the V$K\alpha$ line and of the V$K\beta$ line on the Cr$K\alpha$ line were accommodated using the OVERLAP CORRECTION software. The probe diameter was ~1–2 μm. Natural specimens of olivine (Mg, Si, Fe, and Ni) and chromiferous or manganiferous garnet (Ca, Cr and Mn) were used as standards for olivine. A natural specimen of magnesian chromite (for Cr, Fe, Mg, and Al), manganiferous garnet (Mn), ilmenite (Ti) and synthetic oxides $NiFe_2O_4$ (Ni), $ZnFe_2O_4$ (Zn), and V_2O_5 (V) were used as standards for chromian spinel. Grains of orthopyroxene and hydrous silicates were analyzed using pyrope (Si, Al, Fe), a glass Ti standard (GL-6), chromiferous garnet (Cr), diopside and pyrope (Mg, Ca), manganiferous garnet (Mn), albite (Na), and orthoclase (K). All data were processed with the ZAF method of corrections. The calculated values of detection limit (1σ criterion) are: ≤0.01 wt.% for Ti, Cr, Fe, Ni, Ca, Zn, Mn, and K, and 0.02 wt.% (Na and Al). Special tests [28,29] were done to evaluate the accuracy and reproducibility of the analytical procedures. The sulfide minerals were analyzed at 20 kV and 50 nA using a finely focused beam (~1 μm), the standard Phi-Rho-Z procedure and the following lines (and standards): Fe$K\alpha$, Cu$K\alpha$, S$K\alpha$ ($CuFeS_2$), Co$K\alpha$, Ni$K\alpha$ (synthetic FeCoNi alloy); the slight overlaps of the Fe$K\beta$ line with the Co$K\alpha$ line were corrected.

3. Results and Observations

3.1. Olivine and Olivine–Chromite Parageneses

In the Orthopyroxenite zone, olivine appears sparsely, in quantities distinct from those present in the overlying sequences of Ol-free and Ol-bearing orthopyroxenite (~5–10 vol.% Ol) and harzburgite (~70–80 vol.% Ol). In the Dunite block, olivine grains are extensively altered and replaced by a mixture of serpentine-group minerals, clinochlore, and Mg-rich carbonates. Fresh grains or large relics of Ol grains are preserved in some exposures of dunite documented along the composite profile *e–f*, which is most informative as a cross-section across the major zones of chromitites (Figure 3b). We established the composition of olivine in lode outcrops exposed along the traverses *a–b* and *c–d* (*n* = 46; Figures 3a, 4a and 5a). Values of the Mg# index, i.e., $100Mg/(Mg + Fe^{2+} + Mn)$, in Ol grains vary from 85.7 to 91.0, with a mean of 87.6 along these traverses. These are representative of the entire Orthopyroxenite zone. Contents of NiO and MnO, expressed in weight %, are: 0.26–0.49, mean 0.34, and 0.12–0.24, mean 0.17 wt.%, respectively.
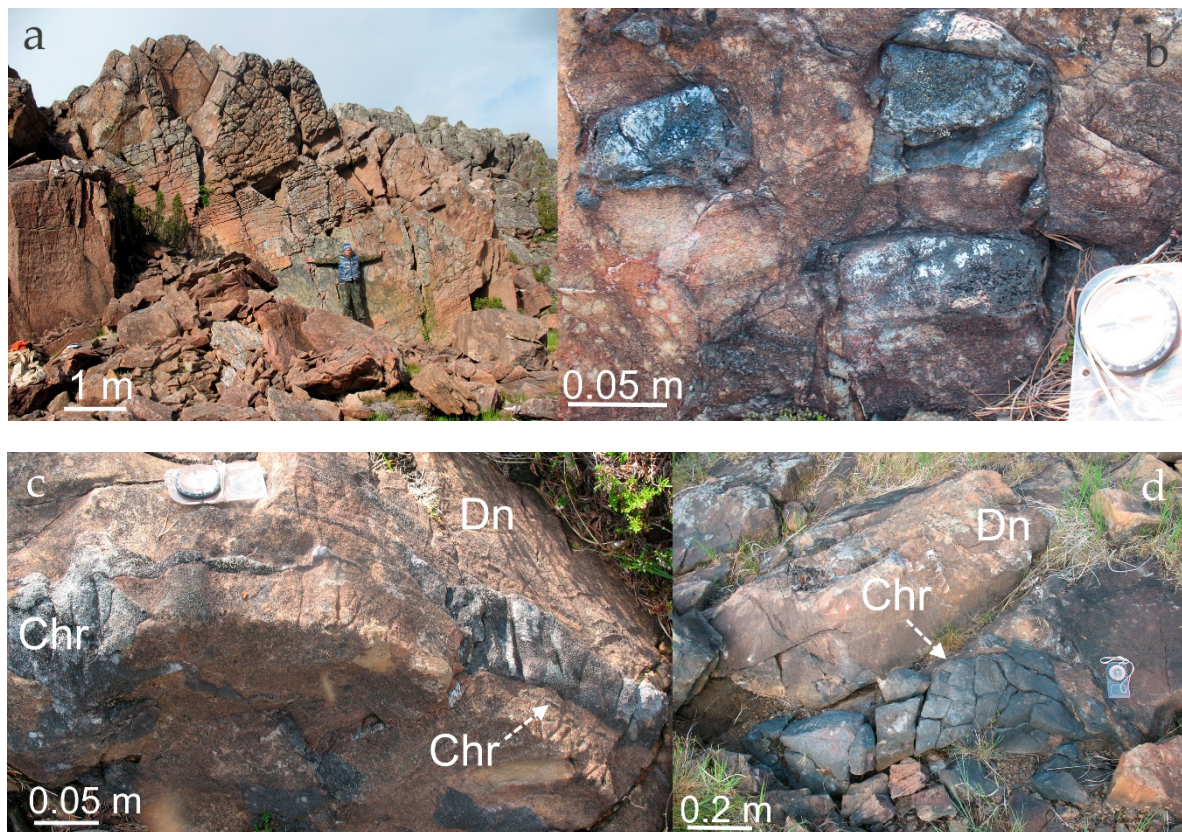
Figure 4. (**a**) One of the lode exposures of ultramafic rocks examined along the traverse *a–b* in the Orthopyroxenite zone at Pados-Tundra. Note the development of a cellular-like parting with shagreen surfaces over the head of S.S. Kramzaev. (**b–d**): Shapes of representative segregations and veins of chromitite (Chr) hosted by dunite (Dn) in the Dunite block.
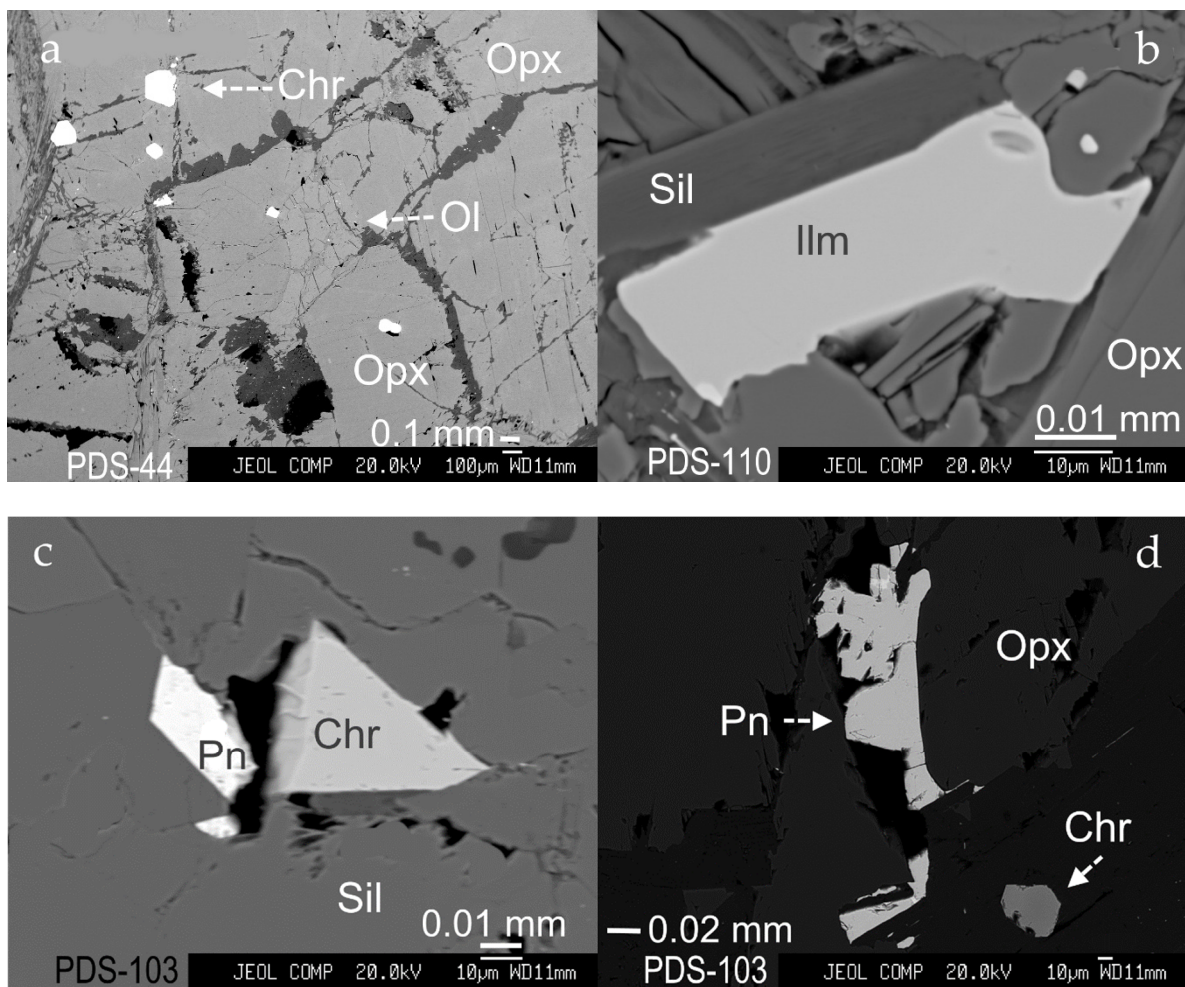
Figure 5. Back-scattered electron (BSE) images show representative textures and associations of ultramafic rocks in the Pados-Tundra complex. (**a**) A droplet-shaped grain of olivine (Ol) in the center is associated with grains of orthopyroxene cumulate (Opx). Subhedral grains of accessory chromian spinel (Chr) are present. (**b**) A grain of magnesian ilmenite (Ilm) occurs at the boundary of an orthopyroxene grain (Opx) and is associated with hydrous silicates (Sil) of deuteric origin, i.e., clinochlore and talc. (**c**) An intergrowth of tiny grains of chromite (Chr) and pentlandite (Pn) at the boundary of silicate minerals (Sil). (**d**) Irregular grains of pentlandite (Pn) occur in association with chromian spinel (Chr); these are located close to the boundary of an orthopyroxene grain (Opx).

The rocks in which grains of Ol were analyzed in the Dunite block are composed of (1) fine-grained olivine (samples PDS-212–215) enriched in disseminated grains of Chr; (2) semi-massive samples of dunite containing chain-like aggregates of Chr grains that are commonly and strongly zoned (PDS-400, 409; Figure 6a,c); (3) Ol–Chr cumulates, in which equigranular crystals of Ol coexist with abundant and well-developed grains of zoned Chr (PDS-405, 432; Figure 6b,d and Figure 7d); and (4) small relics of corroded Ol grains in Ol–Chr rocks enriched in clinochlore. The following ranges of Ol compositions were documented on the basis of 79 data-points that pertain to the Chr-mineralized zones (Figure 3b): Mg# 89.9–93.3, mean 91.5, with 0.32–0.50 wt.% NiO (mean 0.41) and 0.07–0.21 (mean 0.15) wt.% MnO. The notably Mg-enriched compositions are clearly characteristic of the Dunite block, which thus crystallized before the Orthopyroxenite zone.
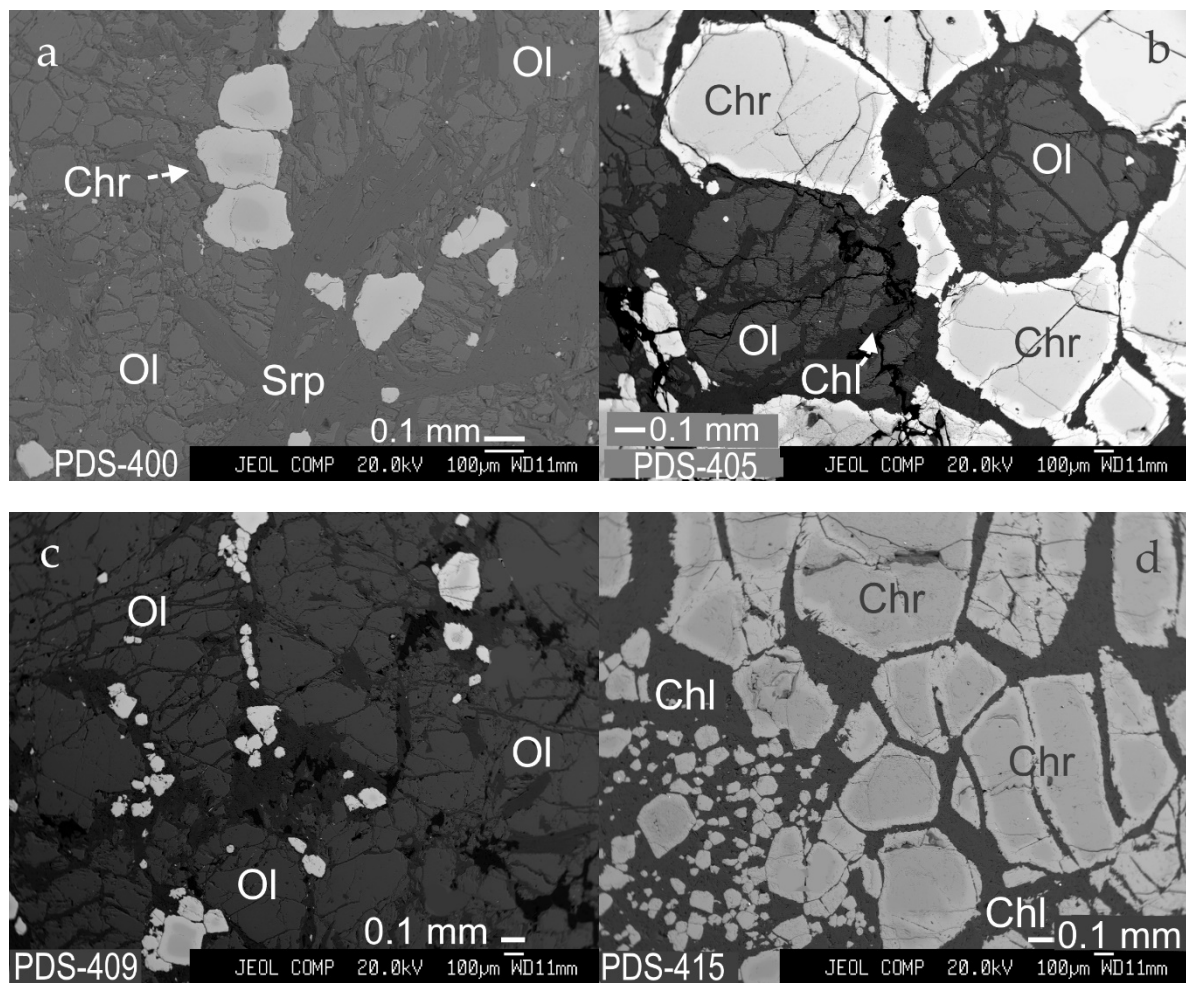
Figure 6. Characteristic textures and associations observed in chromite–olivine cumulates of the Dunite block at Pados-Tundra, as shown in BSE images. Zoned grains of chromian spinel (Chr) with a diffuse rim (bright) form chain-like aggregates or clusters that tend to accumulate and locate in intergranular spaces among the olivine grains (**a,c**). (**b**) shows an interesting example of an equally grained Ol–Chr cumulate. Some grains of zoned chromite (Chr) are also deposited in the space among the Ol grains. (**d**) displays a taxitic chromitite that is composed of two contrasting parts, one of which consists of a micro-aggregate of Chr grains (less than 0.1 mm in size, in the left bottom corner). The labels Srp and Chl (clinochlore) refer to members of the serpentine and chlorite group, respectively.

On the basis of overall variations in Ol, the highest values of Mg# were attained along the contact of the Dunite block in the Chr-mineralized area (Figure 3b). The maximum in Mg# (93.3; #27, Table 1) was documented in sample PDS-415, and about the same level (Mg# 93.0) is present in sample PDS-214 (#19, Table 1). Note that both are located very close to the outer contact, in common with observations made in the Chapesvara sill, in which the maximum (Fo$_{92}$) occurs in the Upper Contact Facies [20].
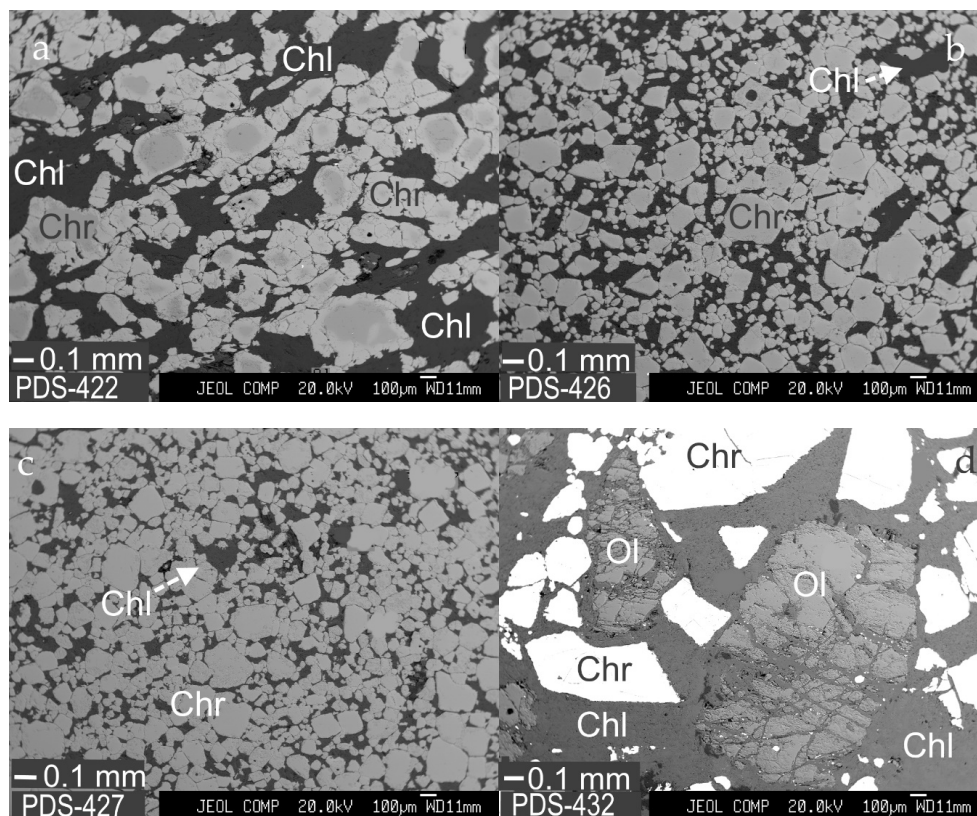
Figure 7. BSE images display characteristic examples of variously mineralized chromitite ores, the grade of which increases from that shown in (**a–c**), in the Dunite block at Pados-Tundra. (**d**) shows well-developed shapes of olivine grains (Ol) associated with chromian spinel (Chr) and clinochlore (Chl).

Table 1. Compositions of olivine in the Pados-Tundra complex.

Sample	Zone	#	SiO₂	Cr₂O₃	FeO	MnO	MgO	NiO	CaO	Total	Fo	Fa	Tep	Mg#
PDS-1		1	41.13	0.02	8.61	0.12	49.82	0.45	0.01	100.16	90.6	8.8	0.1	91.0
PDS-8		2	40.72	0.02	11.39	0.23	47.70	0.29	0.01	100.35	87.7	11.7	0.2	88.0
PDS-41		3	40.77	0.04	11.88	0.16	47.00	0.32	0.01	100.18	87.1	12.4	0.2	87.4
PDS-44		4	40.54	0.03	12.28	0.15	47.18	0.30	0.01	100.47	86.9	12.7	0.2	87.1
PDS-50		5	40.40	bdl	13.30	0.20	45.61	0.32	0.01	99.84	85.5	14.0	0.2	85.8
PDS-54		6	40.74	0.01	12.66	0.19	46.12	0.31	bdl	100.04	86.2	13.3	0.2	86.5
PDS-75		7	41.45	0.01	11.91	0.13	46.56	0.34	0.01	100.41	87.0	12.5	0.1	87.3
PDS-77		8	40.32	bdl	13.13	0.20	46.36	0.31	bdl	100.32	85.8	13.6	0.2	86.1
PDS-80		9	40.69	0.05	12.96	0.19	45.83	0.33	bdl	100.05	85.8	13.6	0.2	86.1
PDS-82	OPXZ	10	40.43	bdl	12.66	0.16	46.68	0.35	0.01	100.30	86.3	13.1	0.2	86.6
PDS-86		11	39.77	0.05	11.22	0.18	48.14	0.33	0.02	99.71	88.0	11.5	0.2	88.3
PDS-88		12	40.70	0.02	11.68	0.17	47.35	0.37	bdl	100.30	87.4	12.1	0.2	87.7
PDS-90		13	40.01	0.04	11.59	0.15	47.26	0.36	0.01	99.43	87.4	12.0	0.2	87.8
PDS-93		14	39.92	0.01	12.27	0.19	47.48	0.37	0.01	100.26	86.8	12.6	0.2	87.2
PDS-97		15	41.20	0.11	9.92	0.18	48.54	0.38	0.01	100.35	89.2	10.2	0.2	89.5
PDS-103		16	39.86	0.03	11.35	0.16	48.07	0.30	0.01	99.78	87.9	11.6	0.2	88.2
PDS-108		17	40.85	0.02	11.87	0.17	47.06	0.35	0.01	100.33	87.1	12.3	0.2	87.4
PDS-111		18	41.03	bdl	10.20	0.14	48.30	0.35	bdl	100.01	89.0	10.5	0.1	89.3
PDS-214		19	41.11	0.01	6.73	0.15	50.97	0.42	0.01	99.39	92.6	6.9	0.2	93.0
PDS-400		20	40.97	0.02	9.54	0.18	49.32	0.37	0.01	100.41	89.7	9.7	0.2	90.0
PDS-403		21	40.94	0.05	9.06	0.18	49.20	0.36	0.01	99.80	90.1	9.3	0.2	90.5
PDS-405		22	40.71	bdl	8.89	0.16	49.92	0.40	0.01	100.09	90.4	9.0	0.2	90.8
PDS-406		23	41.25	0.03	7.48	0.15	50.28	0.41	bdl	99.61	91.8	7.7	0.2	92.2
PDS-409A		24	40.92	0.01	8.57	0.15	49.95	0.39	0.01	100.00	90.7	8.7	0.2	91.1
PDS-409B	DNZ (DB)	25	40.77	bdl	8.72	0.17	49.21	0.38	bdl	99.26	90.4	9.0	0.2	90.8
PDS-409D		26	40.74	0.02	8.83	0.15	49.52	0.37	bdl	99.62	90.4	9.0	0.2	90.8
PDS-415		27	41.61	0.01	6.50	0.07	51.47	0.41	0.01	100.07	92.9	6.6	0.1	93.3
PDS-422		28	40.31	0.05	8.30	0.17	49.91	0.41	bdl	99.14	90.9	8.5	0.2	91.3
PDS-422A		29	40.70	0.07	8.00	0.16	49.74	0.41	bdl	99.06	91.2	8.2	0.2	91.6
PDS-432		30	41.09	0.01	7.02	0.13	51.51	0.50	bdl	100.25	92.3	7.1	0.1	92.8

Note: The label OPXZ is Orthopyroxenite zone, and DB is the Dunite block of the Dunite zone (DNZ); bdl stands for below the detection limit.

Note that the compositions of olivine plot along a single trend of crystallization that extends linearly from the elevated Mg# values in the Dunite block toward notably less magnesian compositions of the Orthopyroxenite zone (Figure 8a). As noted previously [16], the Mg# values of Ol and Opx (and of accessory grains of Chr, as is noted below) tend to decrease toward the central part of the complex. Also, note that the coexisting grains of Ol and Chr behave coherently (Figure 8b), showing a systematic decrease in their Mg# values from dunite of the Dunite block toward the Ol–Opx cumulates of the Orthopyroxenite zone.
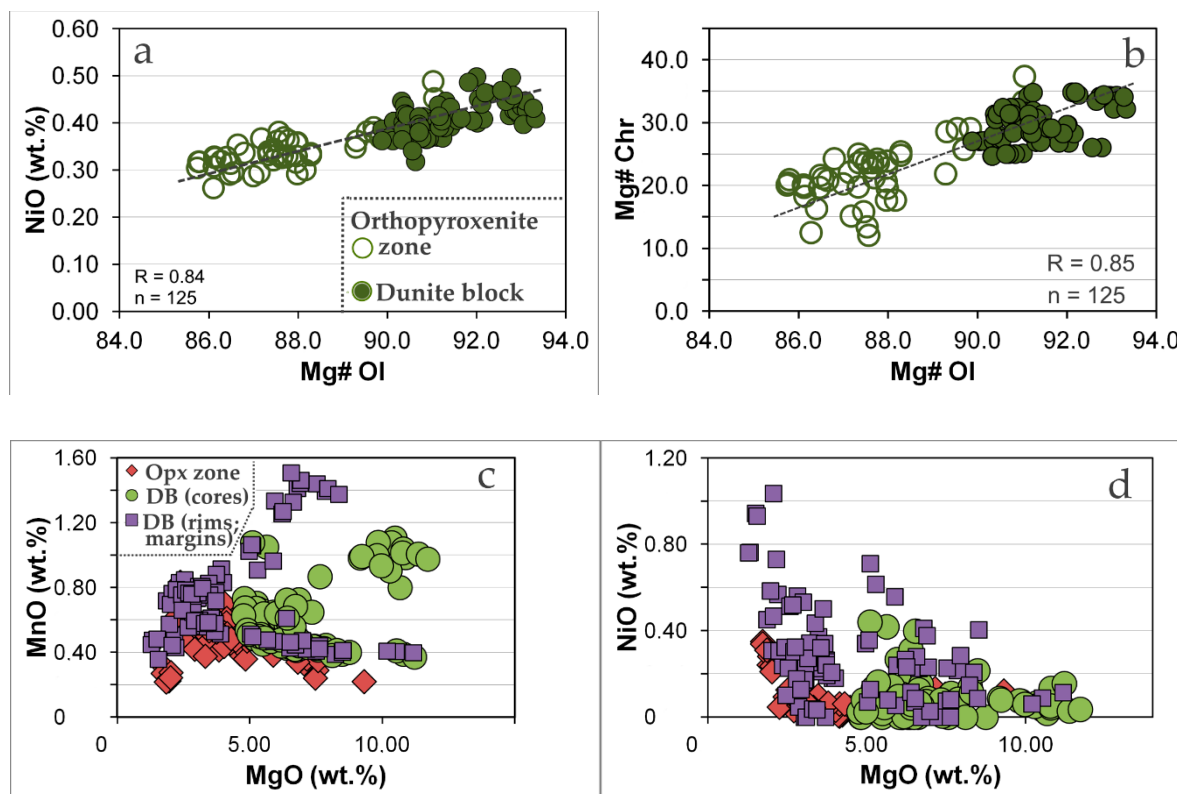
Figure 8. (**a**) Plot of values of NiO (in wt.%) vs. Mg# in compositions of olivine grains (Ol) from the Orthopyroxenite zone (open symbol) and the Dunite block (filled symbol) of the Pados-Tundra complex. (**b**) Sympathetic covariations are observed between Mg# values of the coexisting grains of olivine (Ol) and cores of chromian spinel (Chr) in the Orthopyroxenite zone and the Dunite block. Values of correlation coefficient (R) were calculated on the basis of 125 data-points of Ol compositions, *n* = 125 (Figure 8a), or for a total of 125 pairs of the coexisting Ol and Chr (cores) in Figure 8b. (**c,d**) are plots of MgO (in wt.%) vs. MnO and NiO, respectively, also in weight %, in grains of chromian spinel (Chr) of the Pados-Tundra complex. Accessory grains of Chr analyzed in ultramafic sequences across the Orthopyroxenite (Opx) zone are shown as reddish brown filled diamonds. Cores of Chr grains in chromitite and Chr-enriched zones of the Dunite block (DB) are plotted as filled green circles. Rims of zoned grains (or margins in unzoned grains) from the Dunite block are shown as purple squares.

3.2. Compositional Variations of Ol and Chr across Chr-Rich Zones of the Dunite Block

Variations in Mg# values of Ol and Chr analyzed in Chr-mineralized samples along the composite traverse *e-f*, oriented generally from points *e* to *f* (Figure 3a,c), are summarized schematically in Figure 9a–c. Two groups of data points are present; these reflect the increase in Mg# toward the western contact and its systematic increase toward the northern contact of the Dunite block. The Mg# values display a general rise in Mg enrichment in Ol and Chr toward the curved outer contact of the Dunite block. Note that the amount of Mn in olivine displays a clear antipathetic relationship with the Mg# values (Figure 9b). In the associated suite at Khanlauta (Figure 3a), the amount of Mn in Ol also was indicative of two zones, labeled I and II, defined on the basis of Ol–Chr compositions [22].
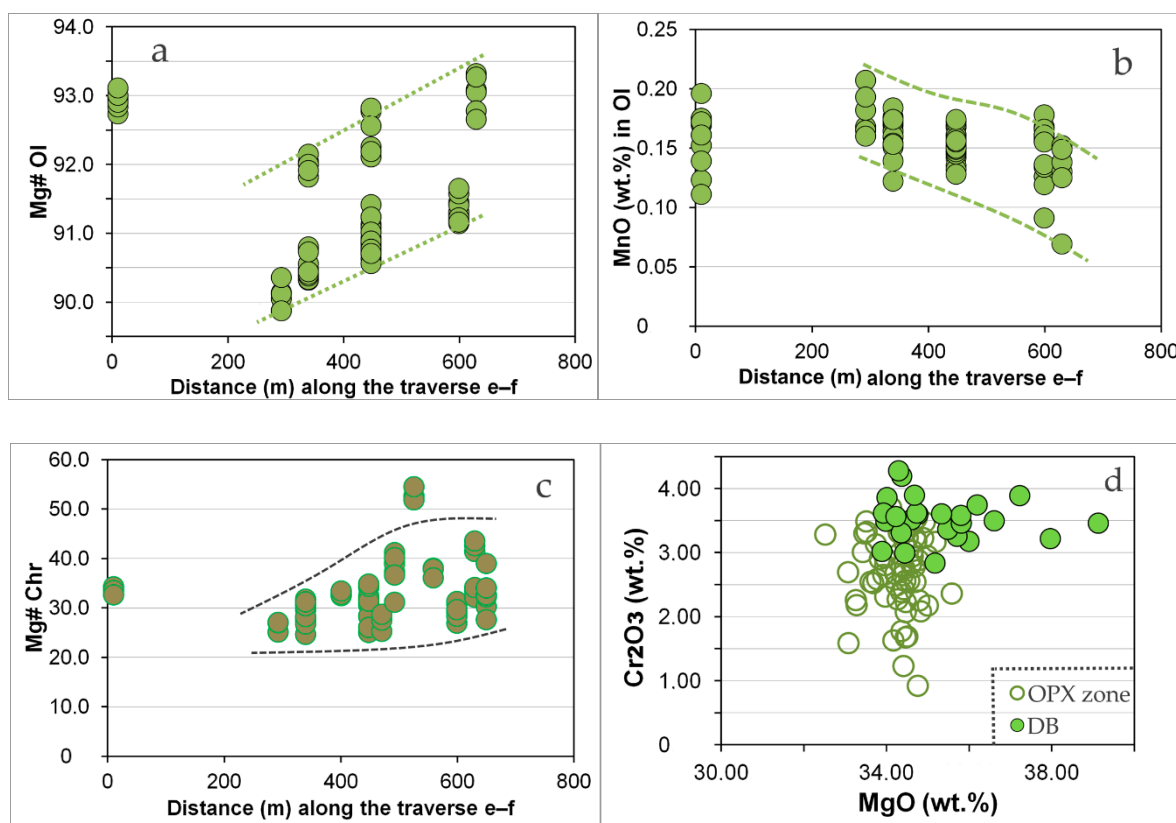
Figure 9. Compositional variations in olivine (Ol) are demonstrated in terms of values of Mg# (**a**) and contents of MnO (in weight %: (**b**); Mg# values of the core of grains of chromian spinel (Chr: (**c**)) are observed across the major zones of chromitite mineralization in the Dunite block and over the length (in meters) of the composite traverse *e–f* (Figure 3a,b). The dotted and dashed lines shown on the plots 9a-c display general trends based on both maximal and minimal values in the observed ranges. (**d**) is a plot of contents of MgO (in weight %) vs. Cr_2O_3 in compositions of clinochlore from ultramafic rocks of the Orthopyroxenite zone (OPX; open symbol) and Dunite block (DB: filled symbol).

3.3. Orthopyroxene, Ca-(Fe-Mg) Amphiboles, Clinochlore and Uncommon Serpentine-Group Mineral

Orthopyroxene, with a Mg-enriched composition, exhibits a fairly limited variability: $Wo_{<0.1–3.0}En_{85.1–91.2}Fs_{8.1–12.5}$ at Pados-Tundra [16]. Two generations of Opx are developed [16], as in the associated Chapesvara sills [20]. The early Opx is primary and magmatic; it is replaced locally by a secondary Opx that is depleted in the non-essential cations (Ca, Al, and Cr). Furthermore, the grains of Opx are preferentially replaced by deuteric assemblages of tremolite–anthophyllite, clinochlore and subordinate talc, whereas the associated grains of Ol typically remain relatively fresh or only slightly affected by alteration [18]. The same phenomenon, distinct from the well-known "uralitization" (developing after clinopyroxene), is also typical of the Chapesvara complex [20].

In addition, at Pados-Tundra, large (up to 4 cm in diameter), elliptical or perfectly spheroidal (in cross-section) grains of Opx were replaced by talc and tremolite (Mg# 95–96), hosted by a matrix of fresh $Fo_{87.5}$ [18]. A similar texture formed by oikocrystic Opx ($En_{86.0}$) was documented in spheroids of the Monchepluton layered complex, Kola Peninsula, Russia [30].

Tremolite is the principal species of amphibole, associated intimately with anthophyllite; they both occur as deuteric assemblages at Pados-Tundra [16]. An overall set of about 200 WDS compositions of tremolite, analyzed at Pados-Tundra, Chapesvara and Khanlauta [16,20,22], display a negative correlation of Na_2O vs. SiO_2 (with a value of correlation coefficient R = −0.8), and a positive correlation of Na_2O vs. Al_2O_3 in weight %, (R = 0.8), which point to a limited extent of the coupled substitution 2Na + 2Al = 2Ca + Si + □.

Clinochlore is one of the major minerals in the Dunite block. It occurs in abundance in all of varieties of chromitite, and in various proportions as Ol–Chr–clinochlore rocks (Figures 6d and 7a–d). Interestingly, relict grains of Opx are entirely absent in such chromitite, in which clinochlore typically is not involved in reactions with Ol grains (Figure 7d). There are thus two possibilities to account for these observations: (1) the Opx extensively reacted with hydrous fluid just after its crystallization as an early magmatic mineral; (2) at least some of the interstitial grains of clinochlore crystallized directly from a fluid phase. Note that crystals of such "primary" clinochlore coexist with intergrowths with Ru-based sulfide–sulfoselenide species of PGM (platinum-group minerals), hosted as micro-inclusions in Chr grains at Pados-Tundra [17]. Inclusions of clinochlore of primary origin were also documented at Chapesvara [19]. Note that grains of clinochlore analyzed in the Dunite block are typically more magnesian and enriched in Cr relative to grains examined in ultramafic successions of the Orthopyroxenite zone (Table 2; Figure 9d). These distinctions are a reflection of the greater primitiveness of rocks of the Dunite block.

Table 2. Compositions of grains of clinochlore in the Pados-Tundra complex.

Sample	Zone	#	SiO_2	TiO_2	Al_2O_3	Cr_2O_3	FeO	MnO	MgO	CaO	Na_2O	K_2O	Total
PDS-5		1	33.66	0.07	13.62	2.88	2.03	bdl	34.78	0.01	0.07	bdl	87.13
PDS-11		2	34.08	0.06	14.63	1.69	2.23	0.01	34.51	0.02	bdl	0.18	87.39
PDS-27		3	33.82	0.03	14.29	3.24	2.21	0.02	34.69	0.03	0.02	bdl	88.35
PDS-30		4	35.24	0.06	13.40	2.23	3.03	0.02	34.47	0.02	bdl	0.01	88.49
PDS-50		5	33.91	0.04	12.68	3.28	3.32	0.02	32.52	0.01	0.02	0.01	85.79
PDS-88		6	34.34	0.01	12.89	3.03	3.49	0.02	34.63	0.02	0.03	bdl	88.45
PDS-94		7	33.24	0.06	14.51	2.18	2.43	0.03	35.00	bdl	bdl	bdl	87.45
PDS-95	OPXZ	8	33.56	0.05	13.95	3.39	2.37	0.03	34.32	0.01	bdl	bdl	87.68
PDS-96		9	32.45	0.06	15.17	2.59	3.13	0.03	33.77	bdl	bdl	bdl	87.19
PDS-103		10	33.14	0.04	13.37	3.13	2.95	0.01	33.75	0.03	bdl	bdl	86.42
PDS-106		11	32.21	0.05	15.46	1.63	2.70	0.02	34.17	0.01	0.01	0.02	86.27
PDS-107		12	33.31	0.05	13.92	2.54	2.42	bdl	34.71	0.01	bdl	bdl	86.96
PDS-108		13	34.39	0.02	12.34	3.71	3.32	0.02	34.11	0.01	bdl	bdl	87.91
PDS-110		14	36.00	0.03	12.81	1.23	2.86	bdl	34.41	0.02	bdl	0.01	87.38
PDS-111		15	34.52	bdl	12.51	3.47	2.77	0.02	34.93	0.02	bdl	0.01	88.25
PDS-403		16	34.45	Bdl	9.09	2.84	3.46	0.02	35.17	0.02	0.02	bdl	85.08
PDS-405		17	33.72	0.01	10.66	3.18	3.07	0.02	35.99	0.02	bdl	bdl	86.67
PDS-406		18	33.31	0.02	11.62	3.37	3.06	0.01	35.48	bdl	bdl	0.01	86.87
PDS-407		19	33.49	0.01	12.62	3.46	2.86	0.01	35.80	0.03	bdl	bdl	88.30
PDS-409		20	33.89	0.01	12.46	3.86	2.88	0.01	34.00	bdl	0.02	bdl	87.14
PDS-409A		21	34.69	0.01	11.80	3.62	3.18	0.04	34.73	0.01	0.01	bdl	88.07
PDS-409B		22	34.66	0.02	10.82	3.59	2.76	bdl	35.80	0.01	0.01	bdl	87.66
PDS-410	DB	23	32.95	bdl	11.44	3.00	2.60	0.01	34.44	0.01	0.01	bdl	84.45
PDS-411A		24	32.64	bdl	10.32	4.28	2.16	0.02	34.29	0.01	bdl	0.01	83.71
PDS-414A		25	34.05	0.02	11.51	3.75	2.70	0.03	36.19	0.01	bdl	bdl	88.24
PDS-415		26	34.33	bdl	9.93	3.50	2.49	0.02	36.60	0.01	bdl	bdl	86.89
PDS-419		27	30.14	0.03	12.20	3.90	1.65	0.02	34.67	0.02	bdl	bdl	82.62
PDS-422		28	35.09	0.02	9.58	3.22	2.70	0.02	37.97	bdl	bdl	bdl	88.60
PDS-430		29	32.25	bdl	11.27	3.56	3.18	0.01	34.22	0.02	0.06	bdl	84.57
PDS-432		30	33.97	0.01	11.74	3.89	2.46	0.02	37.22	0.02	0.04	bdl	89.36

Note: The label OPXZ stands for the Orthopyroxenite zone, and DB refers to the Dunite block of the Dunite zone.

In the present investigation, we document new occurrences of a chromiferous and aluminous member of the serpentine group (Table 3), related to a previously described phase that occurs as the fracture-filling material in olivine in the Dunite block. The serpentine-type phase, likely antigorite, contains 0.20 $Al_{tot.}$ and 0.07 Cr atoms per formula unit (a.p.f.u.) which are likely incorporated via the following scheme: $2\ (^{[VI]}Al + Cr)^{3+} + \square \leftrightarrow 3\ Mg(Fe^{2+})$, with a minor exchange at tetrahedral sites: $^{[IV]}Al \leftrightarrow Si$ [16]. Our data are consistent with this scheme, and indicate that special conditions, crucial for the crystallization of the uncommon variant, were attained episodically in different areas during the postmagmatic stage of formation of the Dunite block. The majority of the grains of serpentine, as well as Mg-rich carbonates (magnesite and dolomite) have common and, as expected, highly magnesian compositions.

Table 3. Compositions of chromiferous aluminous serpentine in the Dunite block at Pados-Tundra.

Sample	#	SiO$_2$	TiO$_2$	Al$_2$O$_3$	Cr$_2$O$_3$	FeO	MnO	MgO	CaO	Na$_2$O	K$_2$O	Total (wt. %)
PDS-400	1	41.91	0.01	3.03	1.51	3.43	0.04	37.57	0.01	bdl	0.02	87.53
PDS-400	2	41.82	bdl	3.55	1.68	3.56	0.03	38.39	bdl	bdl	bdl	89.03
PDS-403	3	41.43	bdl	3.00	1.63	3.40	0.03	38.56	0.01	bdl	0.00	88.05
PDS-409D	4	42.64	bdl	3.26	1.70	3.07	0.02	38.14	bdl	bdl	0.01	88.85
PDS-409D	5	43.33	bdl	2.65	0.51	3.31	0.03	39.69	bdl	0.03	0.01	89.56

							Atoms per Formula Unit (O = 7 a.p.f.u.)							
#	Si	Ti	[IV]Al	[VI]Al	Al$_{tot}$	Cr	Mg	Fe	Ca	Mn	Na	K	$\Sigma_{oct.}$	$\Sigma_{cat.}$	Mg#
1	1.96	–	0.04	0.12	0.17	0.06	2.62	0.13	0.001	0.002	–	0.001	2.97	4.97	95.1
2	1.92	–	0.08	0.12	0.19	0.06	2.63	0.14	–	0.001	–	–	3.02	5.02	95.1
3	1.93	–	0.07	0.09	0.16	0.06	2.67	0.13	0.001	0.001	–	–	3.03	5.03	95.3
4	1.96	–	0.04	0.13	0.18	0.06	2.61	0.12	–	0.001	–	0.001	2.97	4.97	95.7
5	1.97	–	0.03	0.11	0.14	0.02	2.69	0.13	–	0.001	0.003	0.001	2.98	4.98	95.5

Note: The formulae were calculated on the basis of charge balance for O = 7 a.p.f.u.

3.4. Textures, Associations and Compositions of Chr and Magnesian Ilm

The chromitite ore zones, distributed in stratiform fashion in the Dunite block (Figure 2a), are composed of separate podiform and more or less isometric aggregates or veinlet-like segregations enriched in Chr (Figure 4b,c), some of which exceed 0.3–0.4 m in thickness (Figure 4d). Petrographically, these ores consist of chromite or magnesiochromite + olivine + clinochlore rocks hosted by dunite to harzburgite.

In this study, three major types of Chr occurrences at Pados-Tundra were examined. (1) Accessory grains of Chr are present sporadically in the Orthopyroxenite zone (along the profiles *a–b* and *c–d*) as separate grains (Figure 5a,d), commonly subhedral or, in some cases, intergrown with pentlandite (Figure 5c). (2) Cores of zoned grains (Figure 6a–d) are a prominent characteristic of the majority of Chr grains in ore zones of the Dunite block (profile *e–f*, Figure 3a,b). Analytical results are presented for the central portions of unzoned grains of Chr, although these are strongly subordinate to the zoned grains. (3) We also provide data on rims or peripheral zones of zoned grains of Chr, and also the margin in unzoned grains that occur in the Dunite block.

In the chromitite zones of the Dunite block, the amount of Chr may attain or even exceed 80% by volume (Figure 7c). Note that fine-grained textures prevail in the chromitite specimens; grain sizes of Chr vary from <0.1 to 0.3 mm, with the presence of microgranular occurrences of Chr related to some taxitic or banded ore-bearing varieties (Figure 7a–c).

Compositional variations of accessory grains of Chr were evaluated in the overlying Opx–Ol cumulates (mostly orthopyroxenite and olivine orthopyroxenite) along the Orthopyroxenite zone (Table 4). These results show a clear tendency of an overall decrease in Mg# values toward the center of the magmatic complex. The same character of cryptic variations was previously noted for Ol and Opx [16].

In Figures 10 and 11, we examine compositional variations and differences existing among various associations of Chr on the basis of our sets of WDS data collected for the following occurrences: 1) accessory grains of Chr in the Orthopyroxenite zone (a total of 67 data-points; *n* = 67), 2) cores of zoned or unzoned grains of Chr in chromitite zones of the Dunite block (*n* = 90), and 3) rims (or margins of unzoned grains) in chromitite zones of the Dunite block (*n* = 90). Selected results of these sets are presented in Tables 4–6.

Table 4. Compositions of accessory grains of chromian spinel from ultramafic sequences of the Orthopyroxenite zone in the Pados-Tundra complex.

Sample	#	TiO$_2$	Al$_2$O$_3$	Cr$_2$O$_3$	FeO (tot)	FeO (calc)	Fe$_2$O$_3$ (calc)	V$_2$O$_3$	MnO	MgO	NiO	ZnO	Total (wt.%)	Mg#	Cr#	Fe^{3+}#
PDS-1	1	0.16	14.48	50.31	27.36	23.42	4.38	bdl	0.38	6.70	0.06	0.49	100.37	33.4	70.0	14.4
PDS1A	2	0.13	11.98	54.57	25.49	22.17	3.69	0.04	0.29	7.53	0.08	0.23	100.70	37.4	75.4	13.0
PDS-3	3	0.17	12.03	54.13	25.85	22.26	3.99	0.02	0.35	7.42	0.08	0.28	100.72	36.9	75.1	13.9
PDS-3A	4	0.30	14.19	51.11	27.14	23.71	3.81	bdl	0.42	6.57	0.07	0.55	100.72	32.7	70.7	12.6
PDS-5	5	0.10	12.49	53.01	27.08	23.19	4.31	0.01	0.42	6.69	0.05	0.45	100.73	33.5	74.0	14.3
PDS-8	6	0.15	12.73	52.26	29.43	26.12	3.68	bdl	0.66	4.73	0.03	0.41	100.76	23.9	73.4	11.2
PDS-11	7	0.14	12.41	52.78	28.08	24.34	4.15	0.01	0.43	5.91	0.05	0.52	100.73	29.8	74.0	13.3
PDS-27	8	0.85	11.61	49.78	29.85	24.58	5.86	0.17	0.38	5.88	0.11	0.44	99.66	29.6	74.2	17.7
PDS-27	9	0.27	12.29	53.13	26.84	23.16	4.09	0.13	0.35	6.89	0.07	0.33	100.72	34.3	74.4	13.7
PDS-41	10	0.30	11.21	52.63	30.48	26.32	4.61	0.10	0.39	4.65	0.04	0.45	100.69	23.7	75.9	13.6
PDS-41A	11	0.25	11.06	51.95	30.26	25.82	4.94	0.12	0.43	4.71	0.04	0.43	99.75	24.2	75.9	14.7
PDS-44	12	0.32	11.04	51.91	30.29	26.35	4.37	0.12	0.46	4.27	0.04	0.50	99.40	22.1	75.9	13.0
PDS-50	13	0.29	10.91	51.35	31.55	26.84	5.23	0.11	0.50	3.94	0.02	0.56	99.75	20.4	75.9	14.9
PDS-54	14	0.31	10.99	52.79	31.06	27.05	4.45	0.16	0.47	4.14	0.02	0.46	100.84	21.2	76.3	12.9
PDS-64	15	0.27	9.77	54.15	30.65	26.46	4.66	0.09	0.59	4.11	0.01	0.81	100.90	21.3	78.8	13.7
PDS-75	16	0.49	9.63	51.96	32.98	27.32	6.29	0.15	0.42	3.84	0.05	0.57	100.73	19.8	78.3	17.2
PDS-77	17	0.22	10.08	53.50	31.13	26.95	4.65	0.15	0.55	3.88	0.04	0.57	100.59	20.1	78.1	13.4
PDS-80	18	0.62	8.27	52.63	34.00	27.66	7.04	0.11	0.59	3.56	0.06	0.43	100.96	18.3	81.0	18.6
PDS-82	19	1.05	6.95	52.01	35.85	28.46	8.21	0.14	0.50	3.18	0.09	0.47	101.05	16.4	83.4	20.6
PDS-82A	20	0.25	9.59	53.31	31.65	26.80	5.39	0.15	0.44	4.02	0.03	0.54	100.52	20.8	78.9	15.3
PDS-86	21	0.23	11.26	52.73	30.24	25.96	4.76	0.12	0.47	4.89	0.02	0.33	100.76	24.8	75.9	14.2
PDS-88	22	0.25	10.62	50.68	33.18	26.82	7.07	0.17	0.52	4.15	0.06	0.40	100.71	21.3	76.2	19.2
PDS-90	23	0.29	11.88	52.07	30.34	26.38	4.40	0.22	0.50	4.68	0.04	0.36	100.82	23.7	74.6	13.1
PDS-90A	24	0.25	11.23	52.42	30.72	26.51	4.68	0.14	0.48	4.47	0.04	0.36	100.58	22.8	75.8	13.7
PDS-93	25	0.16	4.90	51.73	39.65	28.02	12.92	0.05	0.51	2.87	0.06	0.36	101.56	15.2	87.6	29.3
PDS-94	26	0.48	14.07	50.67	26.94	23.10	4.27	0.06	0.36	7.15	0.13	0.39	100.67	35.2	70.7	14.3
PDS-95	27	0.34	16.27	49.64	23.61	20.22	3.77	0.09	0.22	9.31	0.12	0.14	100.12	44.8	67.2	14.4
PDS-95A	28	0.51	15.69	49.20	26.68	23.05	4.03	0.09	0.24	7.47	0.11	0.43	100.81	36.4	67.8	13.6
PDS-97	29	0.40	12.42	51.29	29.10	24.61	4.99	0.21	0.57	5.80	0.06	0.54	100.88	29.1	73.5	15.4
PDS-97A	30	0.24	10.22	52.50	31.01	25.24	6.41	0.13	0.63	5.04	0.06	0.55	101.01	25.8	77.5	18.6
PDS-103	31	0.33	6.71	57.05	31.29	26.87	4.91	0.07	0.53	3.75	0.04	0.47	100.73	19.6	85.1	14.1
PDS-107	32	0.27	12.06	54.06	26.32	23.36	3.29	0.11	0.34	6.81	0.06	0.18	100.53	33.9	75.0	11.2
PDS-108	33	0.37	13.34	49.99	30.51	26.13	4.86	0.08	0.49	4.98	0.05	0.41	100.69	25.0	71.5	14.3
PDS-111	34	0.41	13.44	50.69	28.97	25.13	4.27	0.15	0.47	5.75	0.05	0.29	100.66	28.6	71.7	13.3

Note: These specimens of Chr-bearing rocks were sampled along the traverses *a–b* and *c–d* (Figure 3a). The index Mg# is $100Mg/(Mg + Fe^{2+} + Mn)$. The index Cr# is $100Cr/(Cr + Al)$. The index Fe^{3+}# is $100Fe^{3+}/(Fe^{3+} + Fe^{2+})$.
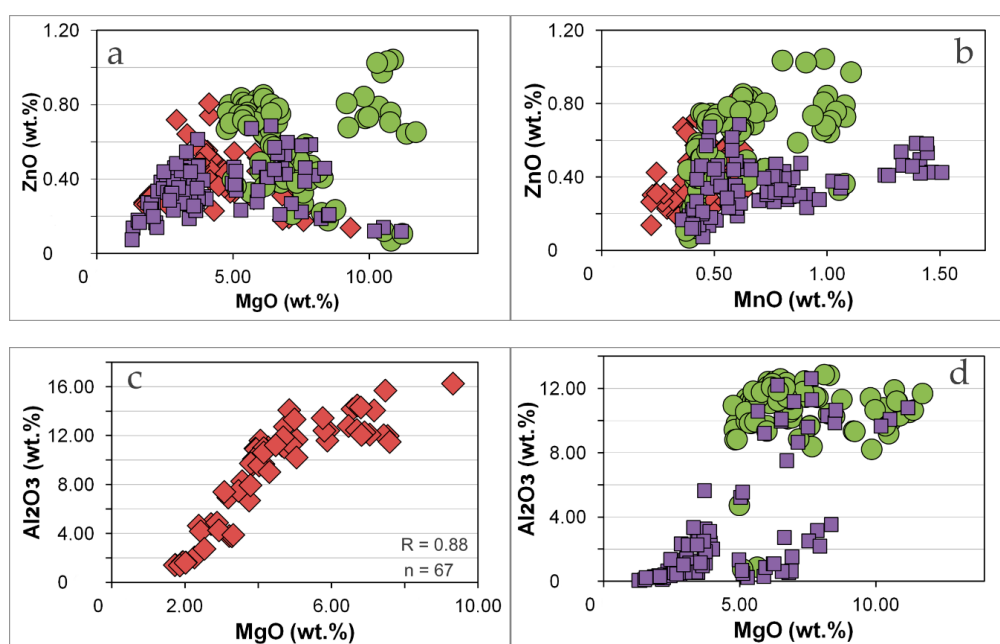
Figure 10. Plots of contents of ZnO vs. MgO (**a**) and MnO (**b**), and Al$_2$O$_3$ vs. MgO (**c,d**), all expressed in weight %, in WDS compositions of chromian spinel from various areas and mineralized occurrences of the Pados-Tundra complex. The symbols are the same as those used in Figure 8c.
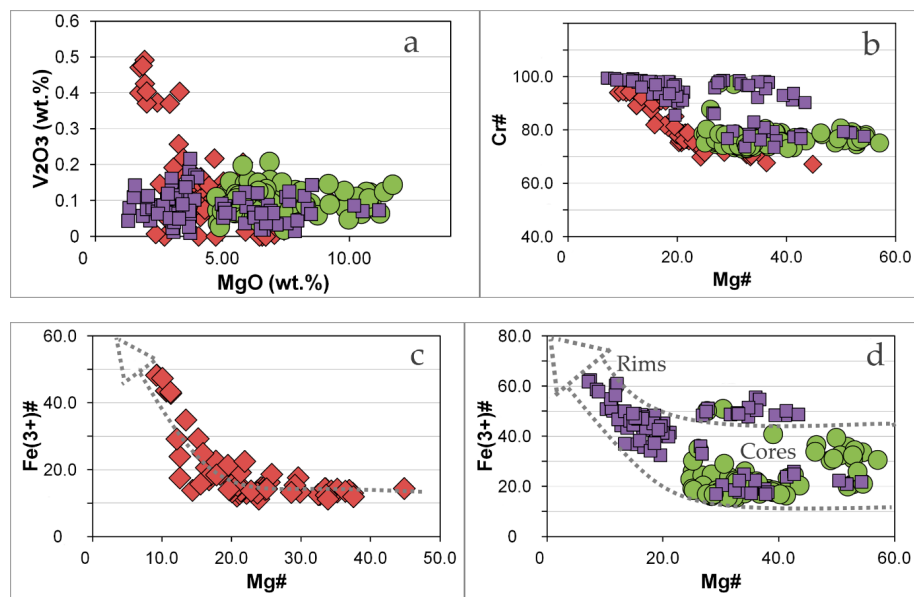
Figure 11. Plots of contents of V_2O_3 vs. MgO, in weight % (**a**), values of the Cr# vs. Mg# (**b**), and Fe^{3+}# vs. Mg# (**c**,**d**), derived from WDS compositions of chromian spinel from various areas and mineralized occurrences of the Pados-Tundra complex. The symbols are the same as those used in Figure 8c.

Table 5. Compositions of cores in grains of chromian spinel from the Dunite block of the Pados-Tundra complex.

Sample	#	TiO$_2$	Al$_2$O$_3$	Cr$_2$O$_3$	FeO (tot)	FeO (calc)	Fe$_2$O$_3$ (calc)	V$_2$O$_3$	MnO	MgO	NiO	ZnO	Total (wt.%)	Mg#	Cr#	Fe^{3+}#
PDS-400	1	0.26	11.09	50.48	31.49	24.71	7.54	0.15	0.67	5.30	0.04	0.84	101.07	27.1	75.3	21.5
PDS-403	2	0.22	11.26	51.77	29.76	24.41	5.96	0.10	0.66	5.48	bdl	0.79	100.64	28.0	75.5	18.0
PDS-405	3	0.29	12.10	51.26	28.43	23.32	5.67	0.09	0.60	6.26	0.11	0.75	100.45	31.8	74.0	17.9
PDS-406	4	0.44	11.49	50.74	30.23	24.11	6.79	0.15	0.65	5.88	0.03	0.83	101.10	29.7	74.8	20.2
PDS-406	5	0.39	11.28	50.72	30.91	24.53	7.09	0.10	0.63	5.56	0.08	0.80	101.19	28.3	75.1	20.6
PDS-407	6	0.19	12.19	51.46	28.70	23.59	5.68	0.10	0.63	6.10	bdl	0.85	100.80	31.0	73.9	17.8
PDS-407	7	0.26	11.79	50.96	28.92	23.40	6.13	0.13	0.62	6.12	bdl	0.83	100.25	31.2	74.3	19.1
PDS-409	8	0.30	10.20	53.92	27.72	22.63	5.65	0.06	0.42	6.91	0.05	0.40	100.53	34.8	78.0	18.3
PDS-409A	9	0.32	11.87	51.10	29.38	23.57	6.46	0.12	0.59	6.35	0.03	0.62	101.01	31.9	74.3	19.8
PDS-409B	10	0.20	10.94	49.29	32.19	24.20	8.88	0.12	0.64	5.53	0.06	0.76	100.61	28.4	75.1	24.8
PDS-409D	11	0.26	12.20	50.31	29.04	23.10	6.61	0.15	0.62	6.39	0.20	0.67	100.48	32.4	73.5	20.5
PDS-410	12	0.19	12.26	51.19	28.12	22.88	5.83	0.14	0.58	6.61	bdl	0.70	100.37	33.4	73.7	18.6
PDS-414A	13	0.29	12.33	51.30	28.49	23.41	5.64	0.10	0.43	6.38	0.31	0.59	100.77	32.3	73.6	17.8
PDS-414A	14	0.19	12.38	51.27	27.45	22.71	5.27	0.11	0.42	6.71	0.15	0.55	99.77	34.1	73.5	17.3
PDS-415	15	0.23	10.92	49.60	30.58	22.61	8.85	0.14	0.51	6.73	0.04	0.49	100.10	34.1	75.3	26.0
PDS-419	16	0.17	11.33	53.23	24.87	19.79	5.64	0.06	0.40	8.75	bdl	0.24	99.59	43.6	75.9	20.4
PDS-422	17	0.24	12.31	51.52	28.67	23.74	5.48	0.09	0.44	6.19	0.09	0.75	100.85	31.3	73.7	17.2
PDS-422A	18	0.24	11.78	51.02	29.19	23.99	5.78	0.20	0.47	5.79	0.14	0.71	100.12	29.7	74.4	17.8
PDS-426	19	0.27	9.70	54.56	26.56	21.49	5.64	0.10	0.42	7.57	0.05	0.27	100.06	38.1	79.1	19.1
PDS-427	20	0.25	10.39	56.41	21.37	16.89	4.97	0.12	0.39	10.80	0.13	0.07	100.42	52.7	78.5	20.9
PDS-427	21	0.26	10.52	56.66	20.66	16.28	4.86	0.06	0.37	11.21	0.15	0.11	100.48	54.5	78.3	21.2
PDS-428	22	0.29	11.44	53.47	26.19	21.36	5.37	0.13	0.45	7.87	0.08	0.47	100.92	39.1	75.8	18.4
PDS-429	23	0.16	12.84	52.63	24.68	20.62	4.50	0.09	0.41	8.28	0.11	0.41	100.06	41.2	73.3	16.4
PDS-429	24	0.19	12.88	52.21	25.37	21.09	4.76	0.13	0.38	8.10	bdl	0.44	100.17	40.2	73.1	16.9
PDS-429	25	0.20	12.49	52.31	26.92	22.29	5.14	0.07	0.44	7.38	0.01	0.39	100.73	36.7	73.8	17.2
PDS-430	26	0.27	9.83	53.80	29.37	24.47	5.44	0.07	0.51	5.40	0.06	0.74	100.60	27.8	78.6	16.7
PDS-430	27	0.18	9.95	53.33	28.92	24.01	5.45	0.11	0.49	5.55	0.05	0.69	99.81	28.8	78.2	17.0
PDS-432	28	0.15	10.71	53.00	28.73	22.59	6.83	0.09	0.47	6.93	0.09	0.55	101.40	34.9	76.8	21.4
PDS-214	29	0.30	11.43	51.16	29.26	22.70	7.29	0.16	0.73	6.86	0.07	0.45	101.13	34.3	75.0	22.4
PDS-216	30	0.39	11.82	51.16	28.22	22.17	6.72	0.15	0.65	7.34	0.08	0.38	100.85	36.4	74.4	21.4
PDS-211	31	0.32	11.24	50.65	29.58	22.95	7.37	0.15	0.72	6.39	0.04	0.80	100.64	32.5	75.1	22.4
PDS-211	32	0.25	11.47	51.15	28.89	22.55	7.04	0.13	0.69	6.73	0.05	0.75	100.81	34.0	74.9	21.9
PDS-213	33	0.34	12.07	50.97	28.77	22.98	6.44	0.12	0.56	6.66	0.07	0.78	100.98	33.5	73.9	20.1
PDS-202	34	0.12	10.31	53.26	22.99	15.24	8.61	0.09	0.99	10.87	0.04	1.04	100.58	54.4	77.6	33.7
PDS-209	35	0.13	11.92	52.09	23.52	16.20	8.14	0.12	0.80	10.67	0.02	1.04	101.12	52.8	74.6	31.1
PDS-208	36	0.12	11.43	51.57	24.78	17.21	8.41	0.13	1.00	9.79	0.08	0.84	100.58	48.9	75.2	30.5
PDS-205	37	0.13	11.21	51.99	24.36	15.96	9.34	0.08	1.04	10.78	0.04	0.76	101.33	53.1	75.7	34.5
PDS-201	38	0.36	11.70	52.88	21.24	14.73	7.23	0.14	0.98	11.71	0.04	0.65	100.43	57.0	75.2	30.6
PDS-203	39	0.13	10.68	52.81	24.99	17.21	8.65	0.05	0.94	9.97	0.06	0.74	101.21	49.5	76.8	31.1

Note: Numbers 1–28 pertain to the profile *e–f*. Numbers 29 and 30 are Chr-enriched specimens of disseminated ores of the Dunite block (DB); #31–33 are segregations in situ in the DB; #34–39 are examples of fragmented chromitites collected in the Dunite block.

Table 6. Compositions of rims or margins in grains of chromian spinel from the Dunite block of the Pados-Tundra complex.

Sample	#	TiO_2	Al_2O_3	Cr_2O_3	FeO (tot)	FeO (calc)	Fe_2O_3 (calc)	V_2O_3	MnO	MgO	NiO	ZnO	Total (wt.%)	Mg#	Cr#	Fe^{3+}#
PDS-400	1	0.31	0.29	37.07	57.43	28.20	32.48	0.06	0.72	1.86	0.45	0.28	101.70	10.3	98.9	50.9
PDS-403	2	0.30	0.37	36.64	57.36	28.01	32.61	0.08	0.70	2.01	0.31	0.27	101.29	11.1	98.5	51.2
PDS-405	3	0.32	0.26	31.47	61.81	27.82	37.77	0.11	0.57	1.97	0.59	0.24	101.11	11.0	98.8	55.0
PDS-405	4	0.30	0.10	24.90	68.26	28.22	44.50	0.11	0.48	1.51	0.94	0.18	101.24	8.5	99.4	58.7
PDS-406	5	0.19	2.82	47.74	43.80	26.21	19.55	0.05	0.77	3.43	0.22	0.47	101.45	18.5	91.9	40.2
PDS-406	6	0.24	1.26	45.72	46.84	26.22	22.92	0.10	0.81	3.18	0.25	0.39	101.09	17.3	96.1	44.0
PDS-407	7	0.16	3.24	47.92	42.91	25.73	19.10	0.01	0.77	3.72	0.26	0.47	101.36	20.0	90.9	40.0
PDS-407	8	0.34	0.79	42.43	50.78	26.61	26.87	0.13	0.74	3.04	0.32	0.33	101.59	16.6	97.3	47.6
PDS-409	9	0.23	9.99	53.99	27.98	22.99	5.55	0.02	0.43	6.51	0.07	0.45	100.22	33.1	78.4	17.8
PDS-409A	10	0.34	0.94	44.40	48.64	26.76	24.31	0.02	0.74	3.04	bdl	0.32	100.86	16.4	97.0	45.0
PDS-409B	11	0.30	0.54	43.43	49.69	26.76	25.48	0.08	0.79	2.59	0.51	0.33	100.80	14.3	98.2	46.2
PDS-409D	12	0.30	0.79	42.58	49.45	26.22	25.82	0.10	0.76	2.81	0.56	0.40	100.34	15.7	97.3	47.0
PDS-410	13	0.28	12.20	50.84	28.40	23.12	5.87	0.12	0.61	6.38	0.11	0.69	100.23	32.4	73.6	18.6
PDS-410	14	0.15	3.28	46.97	43.13	25.63	19.45	0.06	0.72	3.72	0.24	0.39	100.60	20.1	90.6	40.6
PDS-411A	15	0.31	0.68	44.80	45.67	22.86	25.35	0.08	1.07	5.07	0.36	0.37	100.93	27.4	97.8	49.9
PDS-414A	16	0.33	1.14	46.04	46.86	26.65	22.46	0.11	0.56	3.14	0.27	0.27	100.97	17.1	96.4	43.1
PDS-415	17	0.35	0.58	45.67	47.91	26.26	24.06	0.09	0.60	3.38	0.44	0.19	101.60	18.3	98.2	45.2
PDS-415	18	0.25	1.16	47.49	45.38	25.99	21.55	0.14	0.61	3.55	0.32	0.26	101.31	19.2	96.5	42.7
PDS-419	19	0.16	10.32	52.84	26.82	20.42	7.11	0.11	0.39	8.23	0.15	0.19	99.92	41.3	77.4	23.9
PDS-419	20	0.19	9.88	52.77	26.99	19.98	7.78	0.06	0.40	8.49	0.09	0.21	99.84	42.6	78.2	26.0
PDS-422	21	0.34	0.32	29.62	62.11	27.10	38.91	0.11	0.44	2.07	1.04	0.20	100.15	11.8	98.4	56.4
PDS-422A	22	0.33	0.46	40.26	52.60	26.82	28.65	0.09	0.56	2.67	0.52	0.29	100.64	14.8	98.3	49.0
PDS-426	23	0.25	9.61	55.14	26.96	21.84	5.69	0.11	0.41	7.51	0.07	0.23	100.85	37.6	79.4	19.0
PDS-426	24	0.22	7.52	54.82	30.33	22.79	8.38	0.04	0.45	6.72	bdl	0.21	101.14	34.0	83.0	24.9
PDS-427	25	0.25	10.80	56.13	20.96	16.39	5.08	0.07	0.40	11.17	0.11	0.12	100.52	54.3	77.7	21.8
PDS-428	26	0.28	10.61	52.49	29.02	24.07	5.50	0.11	0.48	5.67	0.08	0.67	99.95	29.1	76.8	17.1
PDS-428	27	0.20	11.21	53.54	27.16	22.46	5.23	0.07	0.47	6.99	0.03	0.60	100.79	35.2	76.2	17.3
PDS-429	28	0.25	12.64	52.31	26.49	22.02	4.97	0.13	0.42	7.63	bdl	0.39	100.75	37.7	73.5	16.9
PDS-429	29	0.26	2.33	49.26	43.11	27.21	17.66	0.12	0.65	2.85	0.05	0.46	100.85	15.4	93.4	36.9
PDS-430	30	0.09	3.35	50.76	40.21	26.45	15.30	0.05	0.58	3.29	0.04	0.55	100.44	17.8	91.0	34.2
PDS-430	31	0.16	2.29	50.13	41.89	26.30	17.33	0.09	0.59	3.43	0.03	0.44	100.77	18.5	93.6	37.2
PDS-432	32	0.21	10.11	52.49	29.58	22.97	7.35	0.06	0.46	6.52	0.09	0.57	100.84	33.2	77.7	22.3
PDS-432	33	0.21	5.24	49.45	38.16	24.39	15.31	0.05	0.52	5.03	0.07	0.46	100.72	26.5	86.4	36.1
PDS-202	34	0.31	0.65	45.15	43.58	19.73	26.51	0.07	1.44	6.89	0.38	0.53	101.66	36.7	97.9	54.7
PDS-207	35	0.22	3.16	49.48	36.19	18.65	19.48	0.02	1.40	7.85	0.22	0.59	101.06	41.1	91.3	48.4
PDS-207	36	0.25	2.52	49.78	37.20	19.18	20.03	0.04	1.44	7.53	0.23	0.58	101.56	39.4	93.0	48.4
PDS-208	37	0.32	0.88	48.00	42.01	21.55	22.73	0.08	1.34	5.95	0.24	0.47	101.54	31.6	97.3	48.7
PDS-205	38	0.25	0.64	47.69	42.04	20.42	24.03	0.07	1.51	6.56	0.28	0.43	101.85	34.7	98.1	51.4
PDS-201	39	0.38	2.19	49.31	37.52	18.71	20.90	0.04	1.41	7.95	0.29	0.42	101.60	41.3	93.8	50.1

Note: Numbers 1–33 pertain to the sampling profile *e–f*; #34–39 are specimens of fragmented chromitite ores collected in the Dunite block. Analytical results obtained for rim-like zones are listed in the present Table 6, except for #9, 13, 19, 20, 23–28, and #32, which represent margins of slightly zoned grains or compositionally unzoned grains of Chr.

The compositions of Chromite cores developed in the Dunite block exhibit the maximum values of the index Mg#, i.e., $100Mg/(Mg + Fe^{2+} + Mn)$, which attain 54.5–57.0 (sample PDS-427). The margin of the unzoned grains, as expected, shows about the same Mg# value as the core. In Figures 10a–d and 11a–d, margin compositions are thus plotted in the core-dominant fields. In the rims, which mostly are diffuse, maximum values of Mg# typically vary over the range 42.6–43.4 (e.g., sample PDS-419; Table 6). These values are rather close to the maximum Mg# value (44.8, PDS-95) recorded in the population of accessory Chr grains in the Orthopyroxenite zone (Table 4). One can conclude that the high-Mg cores of the Dunite block crystallized first. The similarity observed in values of Mg# in rims of Chr of the Dunite block with the accessory grains in the Orthopyroxenite zone implies that they crystallized more or less simultaneously under essentially uniform conditions and attained equilibrium in a large volume of melt.

It is fairly unusual that the rim of the zoned grains of Chr in the Dunite block, and even a large number of high-Mg cores, are enriched in the minor elements Mn and Ni to a notably greater extent than grains of accessory Chr in the Orthopyroxenite zone (Figure 8c,d). In addition, these rims are comparatively enriched in both Mn and Ni compared to the cores. Note also that both Ni and V display a tendency of progressive increase in concen-

tration during crystallization of the accessory Chr, followed by the expected decrease in magnesium content with a normal drop in temperature (Figures 8d and 10a).

Another aspect of interest involves the distribution of zinc. It is present as a minor (up to 1.0 wt.%) constituent, preferentially in the highly magnesian core of Chr in the Dunite block (Figure 10a). Moreover, Zn and Mn display a contrast in behavior: Zn exhibits its maximum in the core, whereas Mn is relatively enriched in the rim of zoned grains of Chr (Figure 10b). Evidence of decoupling of Zn from Mn during crystallization of zoned grains of Chr was also documented in zoned sills of Chapesvara [19]. The Mg vs. Al correlation is positive in Chr compositions of the population of accessory grains (Figure 10b), and, with much broader variations, of grains analyzed in the Dunite block (Figure 10d). This correlation reflects the fact that Mg and Al are linked via the spinel component, $MgAl_2O_4$, which is stable at a high temperature in coexistence with forsteritic olivine [31].

Values of the index Chr#, $100Cr/(Cr + Al)$, and the index Fe^{3+}#, $100Fe^{3+}/(Fe^{3+} + Fe^{2+})$, are negatively correlated with the degree of Mg enrichment of Chr (Figure 11c,d). A progressive core-to-rim increase in the Fe^{3+}# is indicated for associations of Chr in the Dunite block. The overall trend of variations, observed in terms of $Cr–Fe^{3+}–Al$ space (Figure 12a), clearly extends toward the rims of zoned Chr grains in the Dunite block, in which the enrichment in ferric iron is extreme.
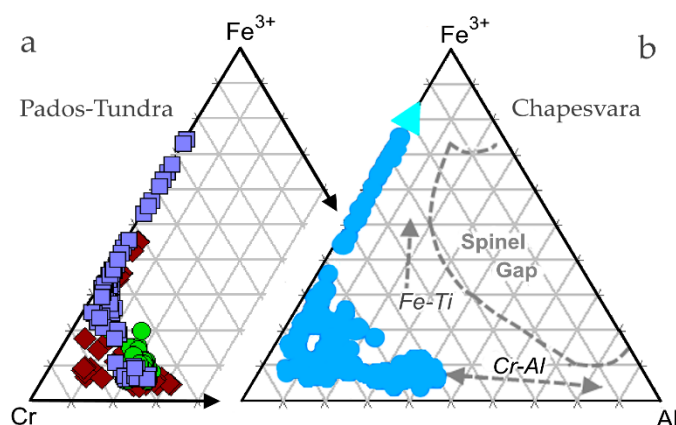
Figure 12. Compositions of chromian spinel from chromite-bearing lithologies of the Pados-Tundra complex (**a**) and of the Chapesvara sills (**b**) [19] in $Cr–Fe^{3+}–Al$ compositional space. The symbols used for Pados-Tundra are the same as those shown in Figure 8c.

Grains of accessory ilmenite (Figure 5b) analyzed in rocks of the Orthopyroxenite zone display a constant composition invariably enriched in the geikilite component (~18 mol.%: Table 7). Interestingly, a grain of ilmenite in sample PDS-30 contains 4.86 wt.% MgO (#1, Table 7), which is notably more strongly magnesian than the associated Chr (2.78 wt.% MgO); this tendency recalls similar occurrences of anomalous Chr–Ilm parageneses documented at Chapesvara and Khanlauta [19,22].

Table 7. Compositions of grains of magnesian ilmenite in the Pados-Tundra complex.

Sample	#	TiO_2	Cr_2O_3	FeO	MnO	MgO	NiO	V_2O_5	Total (wt.%)	Ti	Cr	Fe	Mn	Mg	Ni	Mg#
PDS-30	1	53.31	0.27	39.73	0.57	4.86	0.11	bdl	98.84	0.99	0.005	0.82	0.01	0.18	0.002	17.7
PDS-106	2	54.74	0.06	39.71	0.60	4.78	0.12	0.14	100.16	1.00	0.001	0.81	0.01	0.17	0.002	17.5
PDS-106	3	54.56	0.12	39.79	0.58	4.85	0.13	0.21	100.24	1.00	0.002	0.81	0.01	0.18	0.003	17.6
PDS-110	4	53.35	0.25	39.68	0.43	5.06	0.12	0.17	99.06	0.99	0.005	0.82	0.01	0.19	0.002	18.3
PDS-110	5	53.77	0.11	40.15	0.44	5.04	0.12	0.15	99.76	0.99	0.002	0.82	0.01	0.18	0.002	18.1
PDS-110	6	53.83	0.23	40.41	0.45	5.09	0.12	0.23	100.36	0.99	0.004	0.82	0.01	0.18	0.002	18.2

Note: Al was sought, but not detected (bdl). The formulae were calculated on the basis of charge balance for O = 3 atoms per formula unit; Mg# = $100 Mg/(Mg + Fe^{2+} + Mn)$.

In addition, grains of chromiferous rutile (6.3 wt.% Cr_2O_3) and monazite-(Ce), $(Ce_{0.47}La_{0.38}Nd_{0.10}Pr_{0.03}Sm_{0.01}Ca_{0.01})_{\Sigma1.00}P_{1.00}O_4$, were found as rare phases in specimens of chromitite of the Dunite block.

3.5. Associations of Sulfide Minerals

Occurrences of base-metal sulfides are extremely scarce at Pados-Tundra, thus implying a S-depleted parental magma. Sporadic and tiny grains (Figure 5a,b) of cobaltiferous pentlandite (1.3–3.5 wt.% Co) and subordinate millerite (#6, Table 8) are present. Values of the Ni/Fe ratio, 1.2–1.4, are moderately high (cf. [32]) in pentlandite of the Orthopyroxenite zone; they thus are close to the 0.8–1.1 (with 1.2–1.7 wt.% Co) and 0.9–1.3 (1.0 to 16.7 wt.% Co), the values observed in compositions of pentlandite at Chapesvara and Khanlauta, respectively [20,22]. This ratio is much higher in pentlandite from chromitite hosted by the Dunite block (2.2, #5, Table 8).

Table 8. Compositions of grains of sulfide minerals in the Pados-Tundra complex.

Sample	#		Fe	Ni	Co	Cu	S	Total (wt.%)	Fe	Ni	Co	Cu	ΣMe	S	Ni/Fe
PDS-11	1	Pn	26.87	38.39	1.38	bdl	33.64	100.29	3.70	5.04	0.18	–	8.92	8.08	1.4
PDS-11	2		26.62	38.29	1.39	bdl	33.78	100.08	3.67	5.03	0.18	–	8.88	8.12	1.4
PDS-103	3		28.91	36.23	1.33	0.30	32.63	99.40	4.04	4.81	0.18	0.04	9.06	7.94	1.2
PDS-103	4		28.91	36.56	1.31	0.29	33.09	100.16	4.00	4.81	0.17	0.03	9.02	7.98	1.2
PDS-214	5		19.02	43.94	3.52	bdl	33.52	100.0	2.64	5.80	0.46	–	8.90	8.10	2.2
PDS-214	6	Mlr	0.84	65.48	bdl	bdl	33.19	99.50	0.01	1.03	–	–	1.04	0.96	–

Note: The atomic proportions are based on a total of 17 atoms per formula unit (a.p.f.u.) for pentlandite (Pn) and 2 a.p.f.u. for millerite (Mlr); bdl is below the detection limit.

In chromitites of the Dunite block, various species of PGM are present. The PGM occur as single inclusions or intergrowths ($\leq$1–10 μm) hosted by grains of Chr. Laurite of a low-Os composition is most abundant as intimate intergrowths with grains of "primary" (i.e., non-replacement) clinochlore (>80% laurite grains), followed by Os- and Ir-dominant alloys corresponding to the minerals of osmium and iridium, a Se-rich laurite (members of the RuS_2–$RuSe_2$ series), unnamed $RuSe_2$ and RhTe, and native ruthenium that occurs as micro-(nano)-spherules in framboid-type aggregates [17].

3.6. Geochemical Variations in the Pados-Tundra Complex

Ultramafic rocks analyzed along three cross-sections at Pados-Tundra invariably display high contents of Mg, with a mean value of Mg# 87.6 (this study), which is close to a mean Mg# of 86.7 reported for the zoned Chapesvara-II sill [20] and 86.1 inferred for the Khanlauta flow [22]. The high-Mg compositions are combined with elevated levels of Cr (up to 26.72 wt.% Cr_2O_3: Table 9) in the mineralized specimens of dunite of the Dunite block (Figure 13a); these also are anomalously enriched in Al owing to the abundance of clinochlore (Figures 6d and 7) and to segregations of Chr enriched in the spinel component (Figure 13d). Positive Ni vs. Mg covariations (Figure 13c) are a reflection of the preferred incorporation of Ni in the Fo-rich olivine (Figure 8a).

Table 9. Major element contents of rocks of the Pados-Tundra complex.

Sample	#	SiO_2	TiO_2	Al_2O_3	Fe_2O_3 (tot)	Cr_2O_3	FeO (tot)	MnO	MgO	CaO	NiO	BaO	Na_2O	K_2O	V_2O_5	P_2O_5	SO_3	LOI	Total	Mg#
PDS-1	1	54.54	0.07	1.61	6.53	0.79	5.88	0.13	33.67	1.39	0.09	<0.01	0.12	0.02	0.01	0.01	<0.03	0.05	99.04	90.9
PDS-3	2	54.57	0.07	1.87	6.51	0.80	5.86	0.14	33.34	1.51	0.09	<0.01	0.16	0.01	0.01	0.01	<0.03	0.03	99.14	90.8
PDS-11	3	54.87	0.07	1.69	6.83	0.79	6.14	0.13	33.20	1.39	0.09	<0.01	0.08	0.01	0.01	0.01	<0.03	0.08	99.26	90.4
PDS-27	4	53.77	0.07	1.86	7.12	0.80	6.40	0.13	33.49	1.48	0.08	0.01	0.16	0.02	0.01	0.01	<0.03	0.11	99.13	90.1
PDS-30	5	54.77	0.08	1.50	8.14	0.61	7.32	0.17	32.37	1.37	0.08	<0.01	0.09	0.01	0.01	0.01	<0.03	0.17	99.40	88.5
PDS-41	6	48.50	0.05	1.01	9.94	0.88	8.95	0.16	37.14	0.80	0.15	<0.01	0.07	0.01	0.01	0.01	<0.03	0.38	99.14	87.9
PDS-50	7	48.71	0.05	1.06	9.80	0.88	8.82	0.17	35.83	0.77	0.14	<0.01	0.08	0.01	0.01	0.01	<0.03	1.71	99.25	87.7
PDS-54	8	50.43	0.05	1.12	9.41	0.93	8.46	0.17	35.43	0.98	0.12	<0.01	0.09	0.01	0.01	0.01	<0.03	0.96	99.73	88.0
PDS-64	9	54.62	0.07	1.39	7.23	0.74	6.51	0.15	33.07	1.25	0.09	<0.01	0.08	0.01	0.01	0.01	<0.03	0.55	99.30	89.8
PDS-77	10	46.09	0.05	0.93	10.36	0.95	9.32	0.17	37.50	0.69	0.18	0.01	0.07	0.01	0.01	0.01	<0.03	2.12	99.14	87.6
PDS-80	11	48.98	0.05	1.07	10.04	0.96	9.03	0.17	35.98	0.82	0.15	<0.01	0.01	0.01	0.01	0.01	<0.03	1.07	99.41	87.5
PDS-82	12	50.80	0.05	1.10	9.67	0.83	8.70	0.17	35.08	0.99	0.12	0.01	0.09	0.01	0.01	0.01	<0.03	1.19	100.14	87.6
PDS-88	13	38.29	0.03	0.53	12.81	1.16	11.53	0.17	44.91	0.16	0.37	0.01	0.05	0.01	0.01	0.01	<0.03	1.74	100.26	87.3
PDS-90	14	37.44	0.03	0.55	12.48	1.30	11.23	0.16	44.77	0.26	0.31	0.01	0.05	0.01	0.01	0.01	<0.03	2.35	99.74	87.5
PDS-93	15	37.69	0.03	0.56	12.10	1.36	10.89	0.17	45.67	0.15	0.29	0.01	0.06	0.01	0.01	0.01	<0.03	2.00	100.14	88.0
PDS-212	16	35.49	0.04	1.55	13.31	2.89	11.97	0.15	40.17	0.11	0.28	<0.01	0.05	0.01	0.01	0.01	<0.03	5.26	99.33	85.5
PDS-215	17	25.55	0.26	11.78	10.66	14.38	9.59	0.56	33.08	0.10	0.09	0.02	0.20	0.02	0.09	0.02	<0.03	3.25	100.03	85.3
PDS-400	18	36.95	0.04	1.14	12.42	2.41	11.17	0.17	41.66	0.06	0.27	0.01	<0.05	0.01	0.01	0.01	<0.03	4.57	99.76	86.8
PDS-406	19	32.21	0.06	7.26	10.53	8.08	9.47	0.15	38.54	0.03	0.23	<0.01	<0.05	<0.01	0.02	0.01	0.06	2.77	99.94	87.7
PDS-409	20	22.93	0.13	9.56	14.35	16.92	12.92	0.22	32.42	0.09	0.14	<0.01	<0.05	<0.01	0.04	0.01	0.05	3.02	99.88	81.5
PDS-423	21	23.20	0.14	10.64	12.70	18.82	11.43	0.20	31.46	0.03	0.10	<0.01	<0.05	<0.01	0.05	0.02	0.02	2.51	99.87	82.8
PDS-432	22	14.81	0.19	9.67	24.11	26.72	21.70	0.36	23.66	0.00	0.10	<0.01	<0.05	<0.01	0.05	<0.01	0.02	0.03	99.71	65.7

Note: Results of XRF analysis are expressed in weight percent. The sampling profiles are *a–b* (PDS-1 to # 93) and *e–f* (PDS-212 to #432), which are shown in Figure 3a. Samples #19–22 contain 0.06, 0.11, 0.11, and 0.25 wt.% ZnO. LOI: Loss on ignition. They also contain 0.02–0.04 wt.% Co_3O_4. Mg# = 100 MgO /(MgO + FeO$_{tot}$), expressed as a molar ratio.
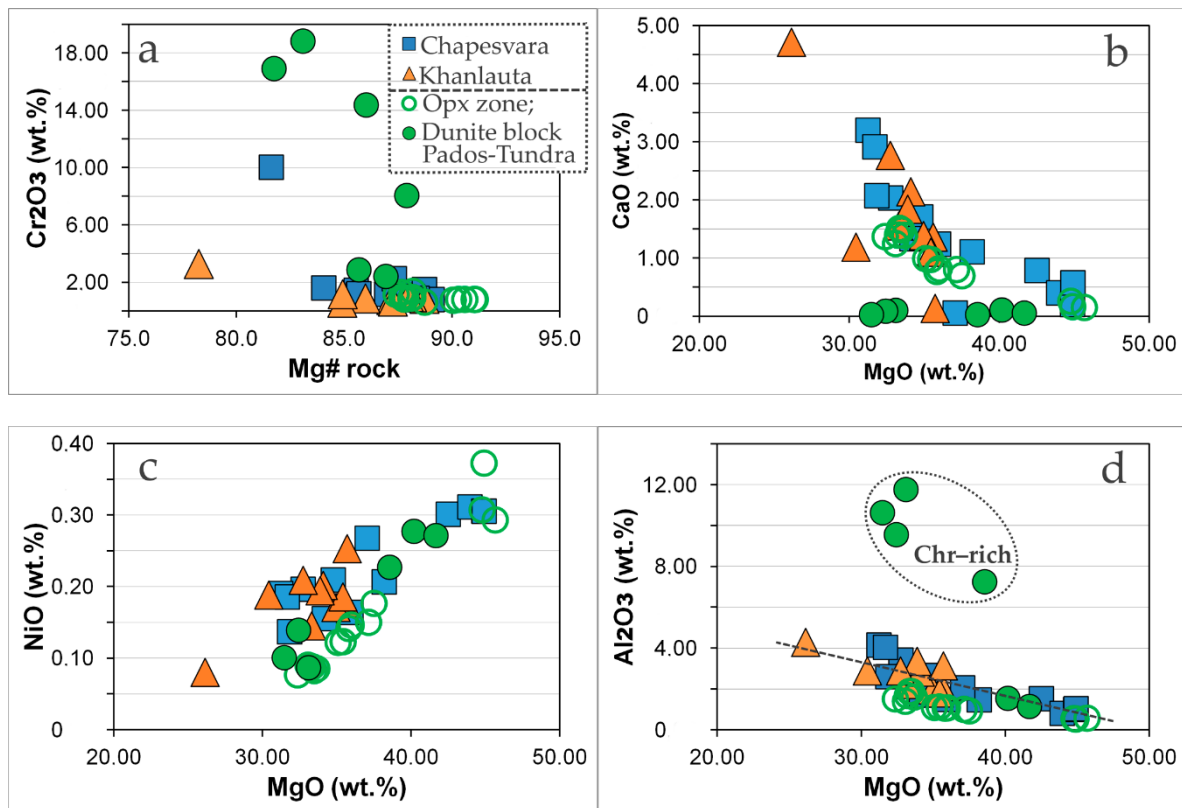
Figure 13. Plot of values of the Mg# index, which is the molar ratio 100 MgO/(MgO + FeO$_{tot}$), vs. contents of Cr_2O_3 in wt.% (**a**), MgO vs. CaO (**b**), NiO (**c**) and Al_2O_3 (**d**) in wt.% in ultramafic rocks of the Pados-Tundra layered complex (shown by green symbols: open circles for the Orthopyroxenite zone and filled circles for the Dunite block), compared with the associated suites of the Chapesvara sill [20], shown by blue squares, and the Khanlauta differentiated flow [22], shown by orange triangles. The field labeled Chr (Figure 13d) shows the mineralized varieties enriched in chromian spinel in the Dunite block at Pados-Tundra.

The Pados-Tundra suite is poor in Ca and Al (Figure 13b,d), as is reflected in the virtual absence of plagioclase and clinopyroxene in these rocks. Owing to a largely incompatible behavior during the crystallization of Ol and Opx, Ca and Al accumulate in a hydrous medium and form abundant grains of tremolite at the expense of the primary grains of Opx.

Among the trace elements, the high-field-strength elements (HFSE) and the rare-earth elements (REE) all correlate sympathetically, e.g., in the selected pairs of Nb vs. Zr, Y vs. V (excluding the Chr-rich varieties that are normally rich in V), and Sm vs. Nd. (Figure 14a–c).
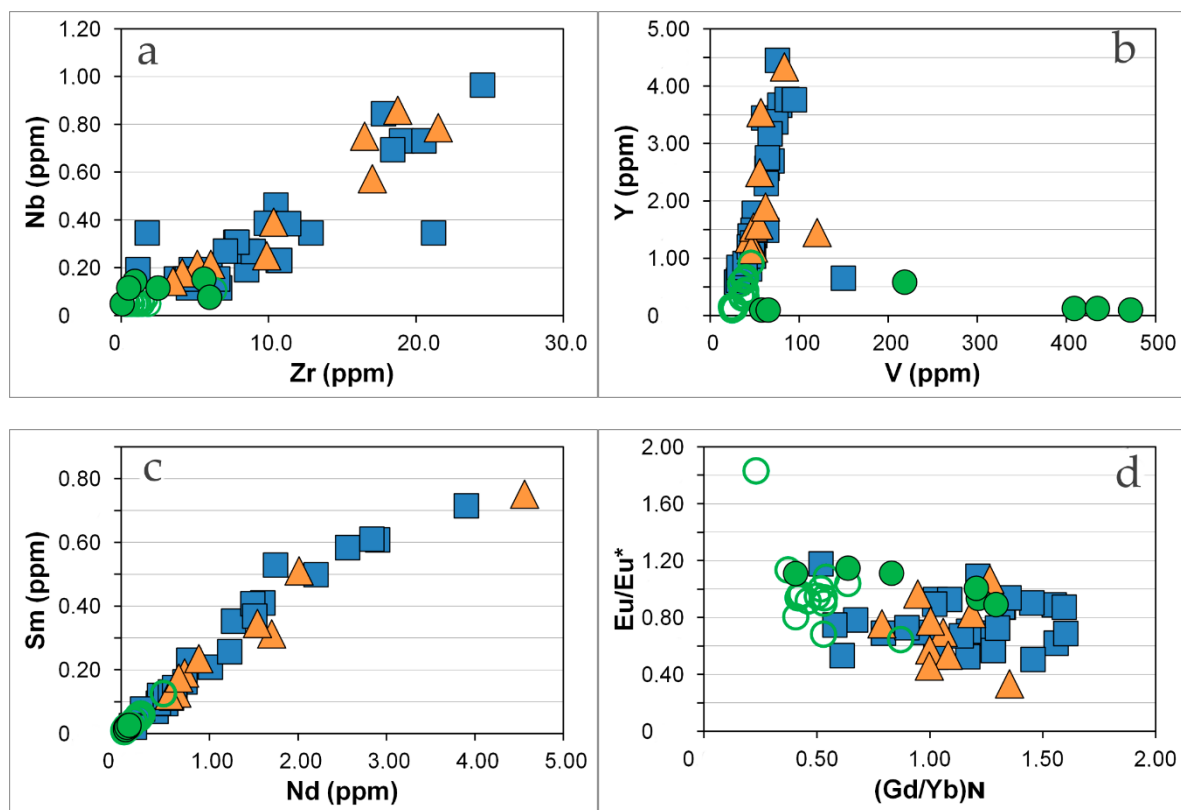
Figure 14. Plot of values of Zr vs. Nb (**a**), V vs. Y (**b**), Nd vs. Sm (**c**), all expressed in ppm, and values of the indexes $(Gd/Yb)_N$ vs. Eu/Eu* (**d**) in ultramafic rocks of the Pados-Tundra layered complex (shown by green symbols: open circles for the Orthopyroxenite zone and filled circles for the Dunite block), and compared with the associated suites of the Chapesvara sill [20], shown by blue squares, and the Khanlauta differentiated flow [22], shown by orange triangles.

Our data indicate that compositions of the ultramafic successions of the Pados-Tundra layered complex, which form a part of a comagmatic shallow plutonic association, display a distinctly stronger primitive character than the Chapesvara and Khanlauta suites [20,22]. Note that $Mg\#_{max}$ values are somewhat greater (Figure 13a), whereas $(Gd/Yb)_N$ values are lower (Figure 14d), with a general depletion in all incompatible elements at Pados-Tundra (Figure 14a–c). The chondrite-normalized spectra are notably primitive in all members of the ultramafic successions at Pados-Tundra, which are closely similar geochemically to the zoned Chapesvara sills, including a rock of the Upper Contact Facies (Figure 15). The latter rock is inferred to represent the closest approximation to the parental magma of Al-undepleted komatiitic composition responsible for the intrusions of the Serpentinite belt [20].
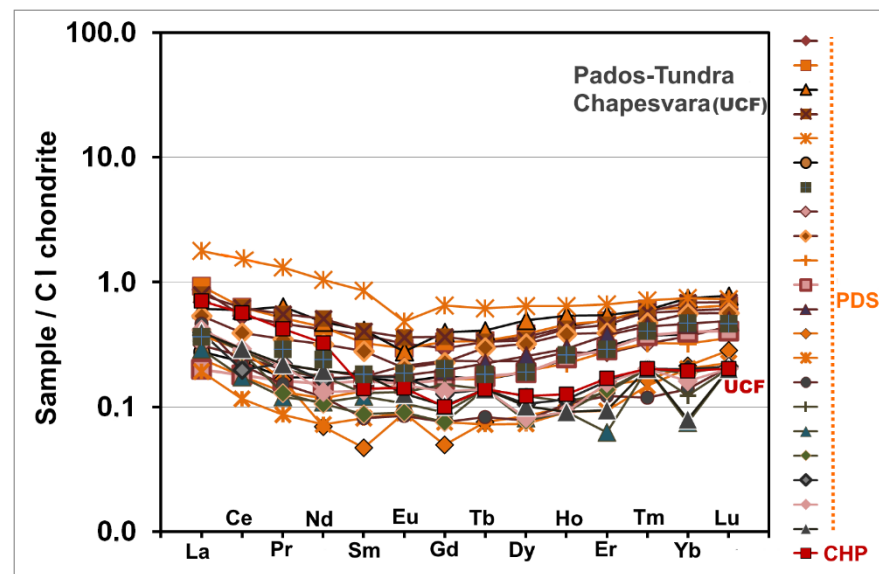
Figure 15. The CI-chondrite-normalized plots of contents of lanthanides in results of whole-rock analyses (ICP–MS) of ultramafic rocks of the Pados-Tundra complex (PDS), in comparison with the Upper Contact Facies (UCF) in the Chapesvara complex, CHP [20]. The CI chondrite-normalizing values by McDonough and Sun [33] were used.

4. Discussion

4.1. Geotectonic Settings and Relationships of the Pados-Tundra Complex with Associated Suites

The Pados-Tundra layered complex and accompanying suites of subvolcanic rocks are located at the boundary of two megastructures of the Fennoscandian Shield: the Paleoproterozoic Lapland granulite terrane (belt) and the Belomorian composite terrane of Archean age [24,34]. The emplacement of the Pados-Tundra complex and large associated ultramafic sills and flows, such as Chapesvara [20] and Khanlauta [22], is related to the development of a collision mélange in the Tanaelv belt (Figure 1), which underlies rocks of the Lapland granulite terrane forming part of the Paleoproterozoic Lapland–Kola orogen.

We believe that the regionally developed komatiitic magmatism resulted in numerous suites of ultramafic compositions in the Serpentinite belt–Tulppio belt (the SB–TB structure) and defines a large igneous province. The emplacement of related complexes of shallow plutonic rocks of highly magnesian composition likely proceeded in response to a large-scale mantle plume. We propose that the central portion of this plume corresponds to major occurrences of dunite—harzburgite—orthopyroxenite complexes: Pados Tundra—Malyi Pados, zoned sills of Chapesvara and Lotmvara, and flows at Mount Khanlauta. The central portions of the plume are expressed in (1) the highly magnesian compositions of these ultramafic rocks, which crystallized from Al-undepleted komatiitic magma [20], (2) the highly magnesian compositions of olivine at Pados-Tundra (Fo_{93}) and Chapesvara (Fo_{92}), and 3) the presence of major deposits of chromite–IPGE-bearing ores hosted by the Pados-Tundra intrusion. In addition, the high values of Cr# in compositions of Chr (Tables 4 and 5, Figure 11b) can also point to the existence of an asthenospheric diapir, i.e., a thermal plume.

In the Russian–Finnish border area, the ultramafic suites (Kareka-Tundra, Termo-Tundra, among others) of the SB–TB structure are clustered within the Paleoproterozoic "Kareka suite" [35]. As noted, the Pados-Tundra and other major representatives were emplaced in relation with the development of the Tanaelv high-grade ductile thrust belt, followed by the development of the collisional mélange (Figure 1). The associated sills of the Chapesvara and Lotmvara complexes are controlled by a system of shear zones of a north-northeasterly strike. Large volumes of komatiitic magma were able to intrude along the subparallel regional shear zones to form the ultramafic sills. Our observations

reveal that the level of magnesium enrichment in the ultramafic suites generally decreases (to about 22.67 wt.% MgO in a whole-rock composition) to the west of the Pados-Tundra complex. Indeed, the Fo values in some specimens of the Mount Kareka-Tundra suite are in the range 80–84 and even 72–77 in relics of olivine grains preserved in ultramafic rocks. Those rocks and their regional equivalents could well be attributed to peripheral areas of the inferred asthenospheric plume.

Close similarities are observed between the geochemical attributes of dunite rocks exposed along the *e–f* traverse (Figures 2a and 3a,b) and close to the boundary of the Dunite block at Pados-Tundra (Tables 9 and 10) and those of the UCF rock of the Chapesvara-II sill; these rocks are close to the parental Al-undepleted komatiitic magma of the Serpentinite belt [20]. The observed trends (Figures 13–15) are consistent with the development of comagmatic series of differentiates of komatiitic magma in a subvolcanic setting. The UCF rock has 37.04 wt.% MgO, 14.88 wt.% FeO_{total}, molar MgO/SiO_2 = 1.8, Mg# 81.3, and contains olivine Fo_{92} [20]. An approximate estimate of parental melt for the Pados-Tundra complex could be made on the basis of sample PDS-409, which is close: 32.42% MgO, 12.92% FeO_{total}, MgO/SiO_2 = 2.1, Mg# 81.5, and Fo_{91}.

Table 10. Minor and trace element contents of rocks of the Pados-Tundra complex.

Sample	#	Sc	V	Cr	Co	Ni	Cu	Zn	Rb	Sr	Y	Zr	Nb	Cs	Ba	La	Ce	Pr	Nd	Sm	Eu	Gd	Tb
PDS-1	1	14.8	38.6	5623.2	75.8	856.0	14.8	40.5	1.30	3.7	0.63	1.10	<0.05	<0.1	<3	0.21	0.33	0.04	0.19	0.06	0.02	0.06	0.01
PDS-3	2	15.8	37.6	5717.3	75.5	888.9	13.8	49.2	1.48	<3	0.63	1.82	<0.05	<0.1	3.0	0.22	0.38	0.05	0.20	0.05	0.02	0.07	0.01
PDS-11	3	15.2	39.9	5643.3	70.9	858.0	6.5	43.5	1.61	<3	0.66	1.62	0.072	<0.1	<3	0.14	0.37	0.06	0.22	0.06	0.02	0.08	0.01
PDS-27	4	15.2	39.0	5751.5	77.5	856.7	14.1	44.3	1.68	3.1	0.63	1.41	0.072	<0.1	3.0	0.19	0.38	0.05	0.23	0.06	0.02	0.07	0.01
PDS-30	5	15.4	46.0	4345.7	91.0	816.8	7.9	48.7	1.82	4.4	0.91	6.30	0.11	<0.1	<3	0.42	0.93	0.12	0.47	0.13	0.03	0.13	0.02
PDS-41	6	11.8	35.1	6241.9	93.3	1445.4	32.3	60.8	2.03	<3	0.35	0.66	<0.05	<0.1	<3	0.07	0.14	0.02	0.08	0.03	0.01	0.03	0.01
PDS-50	7	11.7	39.0	6077.8	86.5	1349.2	14.0	70.0	2.23	<3	0.41	0.62	0.072	<0.1	<3	0.09	0.92	0.03	0.11	0.03	0.01	0.04	0.01
PDS-54	8	12.5	39.9	6224.2	80.3	1192.5	8.5	63.8	2.30	<3	0.44	0.72	<0.05	<0.1	<3	0.07	0.16	0.02	0.08	0.03	0.01	0.05	0.01
PDS-64	9	16.3	34.2	5039.1	77.5	892.8	13.8	54.4	2.12	<3	0.56	1.41	<0.05	<0.1	<3	0.13	0.24	0.03	0.15	0.04	0.01	0.05	0.01
PDS-77	10	9.6	35.9	6217.1	98.2	1591.5	10.8	72.8	2.30	<3	0.31	0.41	<0.05	<0.1	<3	0.06	0.11	0.01	0.05	0.02	0.01	0.03	0.01
PDS-80	11	10.7	40.3	6372.6	83.8	1336.6	9.4	71.9	2.34	<3	0.31	1.12	<0.05	<0.1	<3	0.05	0.11	0.02	0.07	0.02	0.01	0.03	0.01
PDS-82	12	11.9	39.4	5412.3	103.0	1187.2	10.3	57.0	2.09	<3	0.41	0.95	<0.05	<0.1	<3	0.09	0.17	0.02	0.09	0.03	0.01	0.04	0.01
PDS-88	13	4.6	24.0	7535.1	182.0	2951.4	5.5	75.0	2.72	<3	0.16	1.17	<0.05	<0.1	<3	0.09	0.17	0.02	0.03	0.01	0.01	0.01	0.00
PDS-90	14	4.7	27.1	8975.7	178.2	2388.6	5.9	78.9	3.25	<3	0.13	0.29	<0.05	<0.1	<3	0.05	0.07	0.01	0.03	0.01	0.01	0.02	0.00
PDS-93	15	4.5	24.7	9011.8	176.6	2383.0	12.0	76.3	3.47	<3	0.10	0.43	<0.05	<0.1	<3	0.11	0.13	0.01	0.06	0.01	0.00	0.01	0.00
PDS-212	16	9.1	57.4	udl	139.3	2161.7	<5.0	181.1	4.12	<3	0.10	0.07	<0.05	<0.1	<3	0.10	0.17	0.02	0.08	0.02	0.01	0.03	0.01
PDS-215	17	6.7	471.5	udl	222.7	568.41	6.7	1304.0	14.22	17.2	0.10	0.92	0.14	<0.1	<3	0.07	0.11	0.01	0.05	0.02	0.01	0.02	0.01
PDS-400	18	8.8	65.1	15196.0	142.1	2783.3	<5.0	137.4	2.77	<3	0.10	0.49	0.12	<0.1	<3	0.10	0.17	0.01	0.05	0.01	0.01	0.02	0.01
PDS-406	19	3.9	218.3	udl	274.0	2052.9	18.9	978.3	6.31	<3	0.59	2.49	0.12	<0.1	<3	0.09	0.12	0.02	0.08	0.03	0.01	0.03	0.01
PDS-409	20	5.0	408.5	udl	311.7	649.3	7.2	3138.4	6.76	<3	0.13	5.60	0.15	<0.1	5.5	0.10	0.18	0.02	0.06	0.02	0.01	0.03	0.01
PDS-423	21	3.3	434.4	udl	302.2	246.1	7.4	2598.7	6.92	<3	0.13	5.98	0.077	<0.1	5.1	0.09	0.18	0.02	0.09	0.03	0.01	0.02	0.01

Sample	#	Dy	Ho	Er	Tm	Yb	Lu	Hf	Ta	Th	U	$(Gd/Yb)_N$	Eu/Eu*
PDS-1	1	0.09	0.02	0.08	0.01	0.10	0.02	<0.05	<0.05	0.03	<0.02	0.50	0.95
PDS-3	2	0.09	0.03	0.08	0.02	0.10	0.02	<0.05	<0.05	0.02	<0.02	0.53	0.90
PDS-11	3	0.12	0.03	0.09	0.01	0.12	0.02	<0.05	<0.05	0.03	<0.02	0.53	0.68
PDS-27	4	0.08	0.02	0.07	0.01	0.11	0.02	<0.05	<0.05	0.03	<0.02	0.53	0.94
PDS-30	5	0.16	0.04	0.11	0.02	0.12	0.02	0.08	<0.05	0.12	0.04	0.87	0.65
PDS-41	6	0.05	0.01	0.05	0.01	0.06	0.01	<0.05	<0.05	<0.02	<0.02	0.46	0.92
PDS-50	7	0.05	0.01	0.05	0.01	0.08	0.01	<0.05	<0.05	0.10	<0.02	0.43	0.96
PDS-54	8	0.06	0.02	0.04	0.01	0.06	0.01	<0.05	<0.05	<0.02	<0.02	0.64	1.04
PDS-64	9	0.08	0.02	0.06	0.01	0.09	0.01	<0.05	<0.05	<0.02	<0.02	0.41	0.81
PDS-77	10	0.05	0.01	0.04	0.01	0.05	0.01	<0.05	<0.05	<0.02	<0.02	0.52	1.00
PDS-80	11	0.05	0.01	0.05	0.01	0.06	0.01	<0.05	<0.05	<0.02	<0.02	0.42	0.94
PDS-82	12	0.06	0.02	0.06	0.01	0.07	0.01	<0.05	<0.05	0.02	<0.02	0.42	0.96
PDS-88	13	0.02	0.01	0.02	0.00	0.03	0.01	<0.05	<0.05	<0.02	<0.02	0.23	1.83
PDS-90	14	0.02	0.01	0.01	0.00	0.03	0.01	<0.05	<0.05	<0.02	<0.02	0.37	1.14
PDS-93	15	0.02	0.01	0.02	0.00	0.02	0.01	<0.05	<0.05	<0.02	<0.02	0.54	1.08
PDS-212	16	0.03	0.01	0.02	0.01	0.02	0.01	<0.05	<0.05	0.03	<0.02	1.21	0.94
PDS-215	17	0.02	0.01	0.01	0.01	0.01	0.01	<0.05	0.12	<0.03	<0.02	1.20	1.01
PDS-400	18	0.02	0.01	0.02	0.01	0.03	0.01	<0.05	<0.05	<0.03	<0.02	0.40	1.11
PDS-406	19	0.03	0.01	0.03	0.01	0.03	0.01	<0.05	<0.05	0.03	0.03	0.64	1.15
PDS-409	20	0.02	0.01	0.03	0.01	0.03	0.01	0.09	<0.05	0.03	0.06	0.83	1.11
PDS-423	21	0.03	0.01	0.02	0.01	0.01	0.01	<0.05	<0.05	0.06	0.06	1.29	0.89

Note: These values are expressed in parts per million. The label "udl" means values exceeding upper detection limits.

The Mg enrichment in Ol and Chr, indicated by Mg#, generally decreases from 93.3 and 57.0 in the Dunite block of Pados-Tundra (this study) to a $Mg#_{max}$ of 91.7 and 42.5 in the zoned sills of Chapesvara [20], and to 87.9 and 31.9, respectively, in the differentiated flow at Khanlauta [22]. This decrease in the Mg# values is correlated with a decrease in the size or relative volume of the subvolcanic bodies, from Pados-Tundra, to Chapesvara to Khanlauta. These intrusive suites display similar trends of geochemical evolution, showing the closest approach to the parental magma's composition in the early-crystallizing rocks of the Pados-Tundra complex (Figures 13a and 14). The emplacement of these bodies was sufficiently shallow to be expressed in the abundance of micro- to fine-grained textures, the presence of columnar jointing, crystallite-like forms of Ol [22], along with signs of supercooling inferred by the appearance of spheroidal textures [16,18]. Because of the subvolcanic

emplacement, the komatiitic magma could vesiculate vigorously. The crystallization of the anhydrous primary minerals presumably caused the magma to reach saturation in H_2O efficiently. Dissociation of the hydrous fluid in the bubbles and the ensuing loss of H_2 through boiling or diffusion led to the progressive conversion of a fraction of Fe^{2+} to Fe^{3+}. The chromian spinel evolved toward highly Fe^{3+}-enriched compositions (Figure 11c,d and Figure 12a,b). In the $Cr–Fe^{3+}–Al$ diagram, the fields and trends observed for associations of Chr at Pados-Tundra and Chapesvara are very similar, even though the Chr at Chapesvara has more aluminous compositions, which extend along the Cr–Al trend toward the Al apex (Figure 12a,b). The development of highly oxidizing environments appears to be a common characteristic of the subvolcanic complexes of the Serpentinite Belt [16–20,22].

Paragenetic associations of sulfide species are also similar in these suites; they all display a pronounced Ni-enrichment in assemblages of cobaltiferous pentlandite, millerite and heazlewoodite, deposited at $\leq$630 °C, as inferred from mineral syntheses [32]. We believe that the high levels of fO$_2$ prevailing in the ore-forming systems led to the enhanced extraction of other cations (Ni, Co, Cu) substituting for ferrous iron that had become deficient owing to the inferred $Fe^{2+} \rightarrow Fe^{3+}$ conversion. The presence of inclusions and intergrowths with hematite, documented in grains of sulfide mineralization at Khanlauta, provides a direct indication of highly oxidizing conditions during growth [22]. These conditions can be important to explain the general enrichment in Ni and Cu, known widely for sulfide assemblages developed in chromitites, as proposed [36].

4.2. A Brief Comparison with Komatiites, Picrites and Ultramafic Units of Layered Complexes

Most major occurrences of komatiitic volcanism in the shield consist of differentiated flows of komatiitic basalts of the Vetrenyi (or Windy) paleorift belt [37–39]. They have a Paleoproterozoic age (2.4–2.45 Ga), and are contemporaneous with the emplacement of the Burakovsky layered complex, southern Russian Karelia [40,41]. Related suites of (meta)-volcanic (komatiite–picrite) associations also are developed in the Central Lapland greenstone belt in Finland and northern Norway [42]. The latter associations are altered extensively; the Vetrenyi belt suites are thus more informative. The overall variations of Ol compositions are $Fo_{81–89}$ in the Vetrenyi belt [39]; these generally correspond to median values observed in suites of the Serpentinite belt. Puchtel et al. [37] documented a narrow range $Fo_{86.1–89.5}$ in komatiite of the Vetreniy belt and in the cogenetic Vinela dike. The maximum values are significantly greater at Pados-Tundra (Fo_{93}) and in the UCF of the Chapesvara complex: Fo_{92} [20,36]. In addition, suites of the Vetrenyi belt differ in their lower level of whole-rock Mg content and appear to exhibit greater degrees of differentiation relative to the Serpentinite belt. Comagmatic associations of the Vetrenyi belt vary from komatiite sensu stricto (18–27 wt.% MgO) and komatiitic basalt (8–18 wt.% MgO) to andesite–basalt (6–8 wt.% MgO). The weighted average composition of the Vetrenyi belt corresponds to komatiitic basalt having the following composition: 51.45 wt.% SiO_2, 0.62% TiO_2, 12.0% Al_2O_3, 10.4% FeO, 14.15% MgO, 8.96% CaO, 1.7% Na_2O, and 0.46% K_2O [39]. The Mg content increases from 13 to 17 wt.% MgO toward the inferred center of the Vetrenyi belt, thus corresponding to estimated liquidus temperatures of 1370–1440 °C [37]. The authors considered that the juvenile magma of the plume was contaminated by a felsic crustal material to the extent of 4 to 15%. Relative enrichments in Ca and Al are expressed in the common presence in the Vetrenyi belt of plagioclase and clinopyroxene (locally present in variolitic textures); these are very rare in the Serpentinite belt. In addition, levels of Ti (0.4–0.9 wt.% TiO_2) are notably high in the Vetrenyi belt, and contrast with a general depletion of Ti in the Serpentinite belt. Picrites and picrite basalts of the Pechenga and Onega areas, which were emplaced during younger events of volcanic activity (~2.1 Ga), are generally enriched in Ti to a greater extent, i.e., more than 1 wt.% TiO_2 [43]. Interestingly, microspinifex textures are observed not only in komatiitic rocks of the Vetrenyi belt [39], but also in ferropicrite of the Pechenga complex [44]. There is no documented occurrence of such textures in the Serpentinite belt; nevertheless, individual microcrystalline grains of

Ol were recognized in komatiitic rocks at the mount Khanlauta area [22], relatively close to the location of the Pados-Tundra layered complex (Figure 3a).

The characteristics of the UCF rock at Chapesvara and the fine-grained dunitic rocks located along the *e–f* traverse (Figures 2a and 3a,b) and close to the contact of Dunite block of Pados-Tundra (e.g., PDS-409, Tables 9 and 10) are similar to those of most magnesian variants of Archean komatiite, especially those of the Barberton belt in South Africa, which can attain calculated values up to ~35% MgO; chilled margins of komatiite flows display up to 30.9 wt.% MgO [45–53]. Calculations by [51] show that the initial melt of Al-undepleted komatiite at the type locality at Komati has ~30 wt.% MgO and ~12 wt.% FeO, with olivine Fo$_{94}$. The same composition of Ol occurs in the upper chilled margin of the Alexo komatiite flow, Ontario, Canada [46]. A similar value, Fo$_{93}$, was documented close to the contact of the Dunite block at Pados-Tundra (PDS-415; Figure 3b, Table 1). Thus, the inferred melt of the Serpentinite belt is a little more magnesian but has a higher level of iron, which leads to uniform levels of magnesium enrichment in examples of Paleoproterozoic and Archean komatiites.

The very high extent of Mg enrichment in the initial magma of the Serpentinite belt surpasses levels observed in picrites, e.g., [54]. Some Hawaiian picrites have a calculated MgO content of 21.2 wt.% in the initial melt, with an olivine of Mg# ~92 [55]. A more forsteritic olivine (Mg# 93.5) occurs in the Zimbabwe komatiites, which have a more magnesian composition of the inferred initial melt (~26 wt.% MgO), corresponding to eruption at ~1520 °C [52]. Regionally, komatiitic and picritic associations can coexist [42]. In some cases, komatiitic and picritic rocks are not readily distinguished on the basis of their chemical composition [39,42,56]. A komatiitic melt with ~27 wt.% MgO and 0.5 wt.% Cr$_2$O$_3$ that can produce an early-formed Ol with Mg# > 92, inferred as the starting point for the Bushveld layered complex, South Africa [57,58]. Thick series of dunite—peridotite—pyroxenite rocks (olivine Mg# >91) in the lower portions of magmatic chamber are consistent with a parental melt containing at least 19 wt.% MgO [59]. Komatiitic basalt (14.15 wt.% MgO) of the Vetrenyi belt represents the initial magma for the Burakovsky layered complex of Paleoproterozoic age in southern Karelia [39].

4.3. Formation of PGE–Chromite Zones in Relation to Crystallization of the Pados-Tundra Complex

The dunite–harzburgite–orthopyroxenite successions and the zones of PGE–Chr mineralization of the lopolithic Pados-Tundra intrusion formed in a hypabyssal setting from Al-undepleted and highly magnesian komatiitic magma enriched in Fe and Cr; it also produced the zoned Chapesvara sills and other suites in the province [20,22]. The chromitite-bearing Dunite block (Figure 2a) of the Dunite zone is inferred to have formed early and before the crystallization of sequences of the Orthopyroxenite zone, as a consequence of the normal accumulation of grains of high-Fo olivine that appeared first on the liquidus upon cooling close to the country rock. Our data on compositional variations of Chr (Tables 4 and 5) are consistent with previous inferences [16] that the lopolithic intrusion began to crystallize with dunite exposed close to the outer contact and progressively toward the center. The documented trend in levels of Ni is a function of Mg# of olivine compositions (Figure 8a). The coherent relationships of Mg# values in coexisting phases of Ol and Chr (Figure 8b) all point to a normal crystallization of a single batch of komatiitic magma, which proceeded from the early Ol + Chr cumulates of the Dunite block to the later Ol–Opx and Opx cumulates of the Orthopyroxenite zone.

The major ore zones are located in an elongated area extending along the outer contacts of the Dunite block (Figure 16). Thus, they belong to a contact style of PGE–Chr mineralization. We believe that the formation of layers (Figure 2a) composed of chromitite pods and veinlets, i.e., stratiform zones of discrete orebodies of podiform and veinlet-shaped chromitites (≤0.3 m thick), is a consequence of the efficient loss of heat along the curvilinear boundary at the contact (Figures 16 and 17). The expected front of crystallization moved along the curved boundary then toward the internal portion of the block. The documented trends of compositions of Ol and Chr provide evidence of a cryptic buildup

in Mg# (with complementary decrease in levels of minor Mn in Ol) toward not only the northern but also the northwestern boundary at the outer contacts of the Dunite block. These findings are manifested by the laterally oriented variations in compositions of Ol and Chr, which suggest a complementary rise in the extents of Mg enrichment toward the northwestern boundary of the Dunite block (Figure 9a–c).
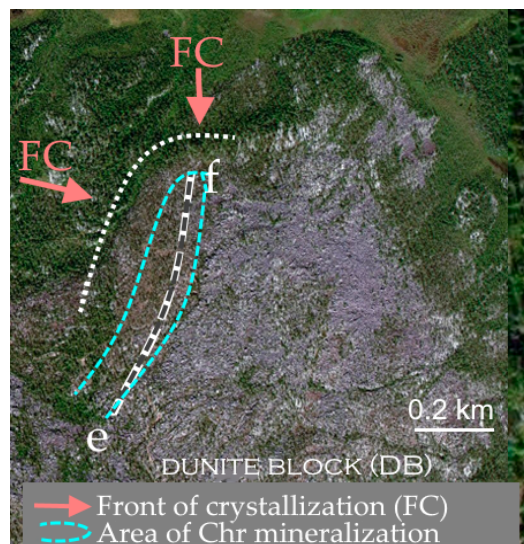
Figure 16. A schematic representation of directions of the inferred front of crystallization during the formation of the Dunite block in the Pados-Tundra layered complex, as shown on a SAS.Planet image. The sampling traverse *e–f* (Figure 3a,b) extends across zones of PGE–chromite (or magnesiochromite) mineralization.
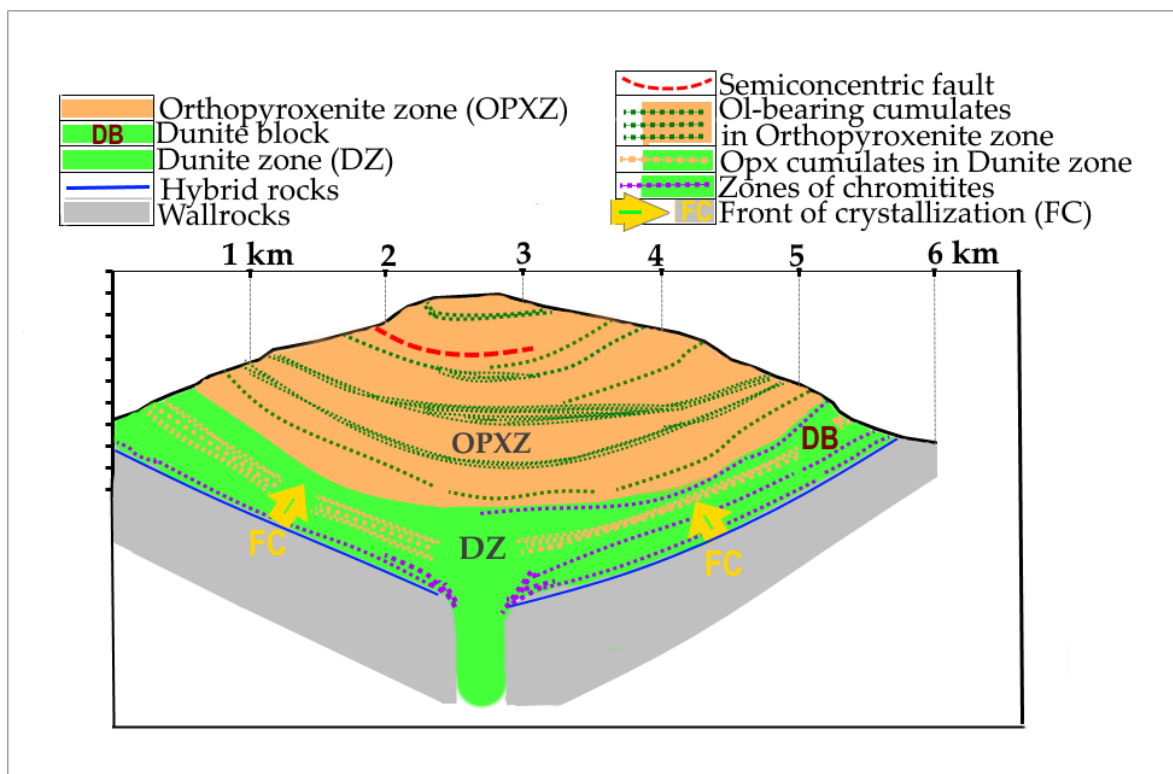
Figure 17. An idealized representation of the geological structure of the Pados-Tundra complex.

We contend that the earliest phase of Ol, having a value maximum Mg# of 93.3, nucleated first close to the outer contact of the Dunite block (sample PDS-415; Figure 3b) in response to cooling. The hypothetical front of crystallization moved along the curved line that is subparallel to the outer boundary of the block (Figure 16). The textural observations clearly imply that the Chr grains and their aggregates were deposited after the crystallization of large volumes of host Ol grains. Indeed, the chromitite segregations commonly display a characteristic shape of veins and apophyses (Figure 4c,d). Grains of Chr typically occupy interstitial spaces or form of chain-like aggregates deposited among Ol grains (Figure 6a,c). In spite of the compatible behavior of Cr that is documented during the crystallization of komatiitic or picritic melts, Cr was clearly incompatible with respect to the crystallizing mass of Ol grains in the Dunite block. Consequently, we expect that levels of Cr, along with other incompatible components (Al, Zn, H_2O, among others), progressively accumulated at the front of crystallization to produce podiform segregations or veins of chromitites arranged in stratiform fashion. Several cycles of Chr deposition, which reflect the position of mappable Chr horizons (Figure 2a), may well correspond to events of episodic Cr-enrichment and deposition along the moving front of crystallization. Rapid crystallization is expected because of the loss of heat at the contact and also the shallow level of emplacement of the lopolith. In addition, the formation of a spheroidal texture and an anomalous variant of serpentine (Table 3) are consistent with the efficient cooling and metastable conditions of crystallization inferred at Pados-Tundra [16,18]. These conditions, which are also implied by the presence of taxitic (Figure 6d) and microgranular textures (Figure 7b,d), likely prevented an effective accumulation of Chr grains. Thus, the chromitite layers are not single and continuous along their strike, but rather are represented by zones of heterogeneously distributed podiform and vein-like segregations of chromian spinel.

The observed spectrum of incompatible elements, such as major Cr and Al, minor Zn, Mn, Ni, Co, S, and relative amounts of the IPGE, thus all became enriched at the crystallizing front. The isolated portions of melt became enriched in magmatic H_2O released and accumulated in the Chr segregations during the massive crystallization of Ol of the dunitic host. Thus, the Chr–Ol–Chl (clinochlore) pods and veinlets crystallized from such a melt saturated in a hydrous fluid under closed-system conditions. As a result, various forms of textures and associations of Chl formed in the PGE-bearing chromitites from portions of H_2O-enriched fluid at a T possibly as high as 880 °C, the upper limit of thermal stability of clinochlore [60]. The abundances of interstitial forms of Chl (Figure 6b,d and Figure 7a–d) can be produced by the replacement of a pre-existing Opx precursor [18]. However, grains of primary Chl are clearly developed in chromitites at Pados-Tundra, as two-phase inclusions of laurite + Chl hosted by grains of Chr. These intergrowths crystallized from microvolumes of H_2O-bearing fluid enriched in Ru, S, and lithophile elements [17]. Note that grains of primary Chl are also present as lamellae crystallized syngenetically along the crystallographically defined growth directions in the host phase of Chr [19].

The intrinsic fugacity of oxygen (fO_2) of the melt and, consequently, the content of ferric iron in Chr phases (Figure 11c,d and Figure 12a) increased progressively during crystallization of the lopolithic intrusion at Pados-Tundra, in common with evolution history of other suites of the belt: Chapesvara, Lyavaraka, and Khanlauta [19,20,22]. Maximal values of fO_2 were attained at the late stage of magmatic crystallization of the chromitites, as is expressed in the abundances of diffuse rims of Chr (Figures 6 and 7a). The highly oxidizing conditions appear to have resulted in the appearance of the anomalous Chr–Ilm parageneses, observed in all three related suites [19,20,22]. The anomalous buildup in Mg# values of Ilm over the coexisting grains of Chr is due to a progressive reduction in relative amounts of Fe^{2+} that is largely oxidized to Fe^{3+}. As noted, we believe that these conditions of pronounced oxidation leading to a deficit in Fe^{2+} account for the deposition of highly Ni–(Co)-enriched phases of sulfide minerals: Co-bearing pentlandite having a high Ni/Fe value (Table 8), millerite, and heazlewoodite at Khanlauta. Indeed, the sulfide intergrowths at Khanlauta involve hematite grains, which indicate the likely levels of fO_2 above the

M–H (magnetite–hematite) buffer [22]. These associations likely formed at a subsolidus temperature, <650 °C, followed by a relative buildup in fS$_2$. The suggested estimates are corroborated by the data acquired from syntheses. These show that pentlandite and its Co-bearing variety are stable at <650 °C; the upper limit of stability of heazlewoodite is up to 556 °C [32], and the β–α inversion in NiS (i.e., millerite equivalent) occurs at 379 °C in the system Ni–S [61]. A high-temperature form of pentlandite, stable up to 865 °C, seems unlikely because of its limited field of stability and its common inversion to pentlandite (low form) with a lowering of temperature [62].

The Chr rims in the chromitites show a relative enrichment in minor Ni and Mn. In contrast, Zn is preferentially partitioned into the core (Figure 8c,d and Figure 10a). This decoupling of Zn from Mn was also previously reported from the Chapesvara complex [19]. The unusual zoning could primarily reflect an elevated level of Zn, accumulated initially in the Cr–Al-enriched isolated portions of melt giving rise to the chromitites. Its content then decreased gradually during crystallization as the melt became exhausted in Zn, unlike Mn or Ni, which displayed a normally incompatible behavior.

The degree of intrinsic oxidation attained by the melt appears to be approximately equivalent at Pados-Tundra and Chapesvara (Figure 12a,b). However, it was notably greater than that implied by the compositions of Chr reported from other deposits in ultramafic-(mafic) complexes, such as at Monchepluton [36,63], Burakovsky [64], Russia, and Kemi, Finland [65]. The highly oxidizing conditions appear to have promoted the formation of sulfoselenide–selenide phases of Ru (S/Se ratio $\leq$ 6) in chromitites of the Dunite block at Pados-Tundra [17]. These are unusual, because extremely low values of S/Se are implied. An oxidizing character of the medium, close to the anglesite–galena buffer [66], is essential to form selenide minerals. The S/Se value of the mantle is 2850–4350 with a mean of ~3250, and the chondritic value is 2500 $\pm$ 270 [67,68]. Relatively low values of S/Se, 190–700, are known in sulfide droplets of the Platinova Reef, Skaergaard complex, east Greenland [69]. Thus, an IPGE-rich sulfoselenide cannot represent a primary phase crystallized from a melt of ultramafic composition, because pure sulfides should form under normal conditions. Also, a magmatic contamination is unlikely to have been involved, because crustal rocks have higher values of S/Se ratios: 3500 to 100,000 [70]. The IPGE-rich phases of diselenide–disulfoselenide compositions at Pados-Tundra rather reflect an ultimate loss of S, causing a critical lowering in S/Se value during the late-stage evolution of H$_2$O-bearing fluid involved in the formation of laurite–clinochlore intergrowths [17]. Note that S is, indeed, more mobile than Se in hydrothermal fluids, being preferentially incorporated into aqueous fluids [71,72]. Degassing may also have been a factor.

5. Conclusions

The Pados-Tundra layered complex is the largest intrusion in the Serpentinite belt–Tulppio belt (SB–TB); it is composed of associations of hypabyssal plutonic rocks crystallized from an Al-undepleted komatiitic magma [20]. This complex is considered to have been emplaced above the central portion of a large-scale mantle plume. The SB–TB plume is reflected by regional suites of dunite–harzburgite–orthopyroxenite developed in the Fennoscandian Shield. A central location over the inferred plume is consistent with: (1) the highly magnesian composition of comagmatic series of rocks; (2) maximum values of Mg# in Ol (93.3) and Chr (57.0), documented in the Dunite block of Pados-Tundra, even greater than Mg#$_{max.}$ of 91.7 and 42.5 in the Chapesvara sills [19,20]; (3) the presence of major chromite–IPGE-enriched zones hosted by the Dunite block of the Pados-Tundra intrusion, and 4) the high values of Cr# in compositions of Chr grains.

The subvolcano-plutonic association of the Serpentinite belt, involving the layered Pados-Tundra complex and zoned Chapesvara sills, crystallized from a primitive, Al-undepleted and highly magnesian komatiitic magma, which is unusually enriched in Fe and Cr. This magma compares well with most magnesian varieties of Archean Al-undepleted komatiite of the Barberton belt in South Africa. Thus, we presume that injections of a Paleoproterozoic komatiitic magma can exhibit the same and very high level of Mg

enrichment as do the typical examples of Archean komatiite. In addition, the inferred parental melt of the Serpentinite belt, estimated on the basis of the UCF rock of the Chapesvara–II sill (i.e., 37.04 wt.% MgO, 14.88 wt.% $FeO_{total.}$) likely represents the most magnesian komatiitic melts in the Fennoscandian Shield.

The association of the Pados-Tundra layered complex and its satellite sills and flows is distinguished by elevated mean values and maximal extents of Mg content. These values and maximal Fo contents in olivine (Fo_{93} at Pados-Tundra and Fo_{92} at Chapesvara) notably surpass those known in the Vetrenyi belt ($Fo_{\leq 89.5}$) and komatiite–picrite associations of the Central Lapland belt of northern Finland and Norway. These distinctions may well point to a more pristine and juvenile character, and imply greater depths of magma generation of the highly magnesian komatiitic melt inferred for the SB–TB megastructure.

In the lopolithic Pados-Tundra intrusion, dunite began to crystallize from a single batch of komatiiic magma close to the outer contact and progressed toward the center. The early Ol + Chr cumulates of the Dunite block gave way to the later Ol–Opx and Opx cumulates of the Orthopyroxenite zone.

The PGE–Chr mineralization in the Dunite block formed as a consequence of intense cooling along its boundary. The earliest olivine ($Mg\#_{max.}$ 93.3) nucleated close to the outer contact. A hypothetical front of crystallization moved along the curved line parallel to the outer boundary, as indicated by vectors in Ol and Chr compositions, which veer toward the northwestern boundary of the Dunite block. Grains and aggregates of Chr were deposited after crystallization of large volumes of host Ol grains. Levels of Cr, along with Al, Zn, H_2O, and other incompatible components, progressively accumulated at the front of crystallization to produce podiform segregations or veins of chromitites arranged in stratiform fashion. Repeated cycles of Chr deposition reflect events of episodic enrichment in Cr and deposition as podiform or vein-like Chr segregations along the moving front of crystallization.

The incompatible elements include major Cr and Al, minor Zn, Mn, Ni, Co, S and the IPGE; they became enriched at the crystallizing front, in isolated portions of melt enriched in magmatic H_2O accumulated owing to the massive crystallization of anhydrous minerals. The Chr–Ol–Chl pods and veinlets at Pados-Tundra formed from such H_2O-rich melt; clinochlore crystallized at a $T \leq 880\,°C$, i.e., the upper limit of its thermal stability [60]. Grains of laurite, $Ru(S,Se)_2$, occur as two-phase laurite + Chl inclusions hosted by grains of Chr that crystallized from microvolumes of H_2O-bearing fluid. Grains of primary Chl are also present as lamellae crystallized syngenetically in Chr at Chapesvara [19].

The intrinsic fugacity of oxygen of the melt and, consequently, the content of Fe^{3+} in Chr, increased progressively during crystallization at Pados-Tundra and in the other suites of the belt: Chapesvara, Khanlauta and Lyavaraka [19,20,22]. Because of their shallow emplacement, the komatiitic magma could vesiculate vigorously, promoting the loss of H_2 and buildup in fO_2 and, correspondingly, the conversion of a fraction of Fe^{2+} to Fe^{3+}. The oxidizing conditions resulted in the appearance of the anomalous Chr–Ilm parageneses, observed in all three related suites [19,20,22]. In addition, Zn is preferentially partitioned into the core of Chr grains, whereas the Chr rims show relative enrichments in minor Ni and Mn. A decoupling of Zn from Mn is implied, as was reported from the Chapesvara complex [19].

We report a pronounced enrichment of Ni in assemblages of cobaltiferous pentlandite with a high Ni/Fe value, millerite, and heazlewoodite at Khanlauta, likely deposited at $\leq 630\,°C$. The high levels of fO_2 possibly led to the enhanced extraction of other cations (Ni, Co, Cu), substituting for ferrous iron that had become deficient. The presence of intergrowths with hematite in grains of Ni-rich sulfide mineralization at Khanlauta provides a direct indication of highly oxidizing conditions, and the likely levels of fO_2 were above the M–H (magnetite–hematite) buffer [22]. The highly oxidizing conditions appear to have promoted the formation of sulfoselenide–selenide phases of Ru in chromitites of the Dunite block at Pados-Tundra [17].

The attainment of a high degree of oxidation during crystallization of a parental unevolved komatiitic magma accounts for the key characteristics of Pados-Tundra and related suites of the SB–TB megastructure.

References

1. Garuti, G.; Pushkarev, E.V.; Thalhammer, O.A.R.; Zaccarini, F. Chromitites of the Urals (part 1): Overview of chromite mineral chemistry and geo-tectonic setting. *Ofioliti* **2012**, *37*, 27–53.
2. Pushkarev, E.V.; Anikina, E.V.; Garuti, G.; Zaccarini, F. Chromium-Platinum deposits of Nizhny-Tagil type in the Urals: Structural-substantial characteristic and a problem of genesis. *Litosfera* **2007**, *3*, 28–65. (In Russian)
3. Zhang, P.-F.; Zhou, M.-F.; Malpas, J.; Robinson, P.T. Origin of high-Cr chromite deposits in nascent mantle wedges: Petrological and geochemical constraints from the Neo-Tethyan Luobusa ophiolite, Tibet. *Ore Geol. Rev.* **2020**, *123*, 103581. [CrossRef]
4. Hulbert, L.J.; von Gruenewaldt, G. Textural and compositional features of chromite in the Lower and Critical zones of the Bushveld Complex south of Potgietersrus. *Econ. Geol.* **1985**, *80*, 872–895. [CrossRef]
5. Naldrett, A.J.; Kinnaird, J.; Wilson, A.; Yudovskaya, M.; McQuade, S.; Chunnett, G.; Stanley, C. Chromite composition and PGE content of Bushveld chromitites: Part 1—the Lower and Middle Groups. *Appl. Earth Sci.* **2009**, *118*, 131–161. [CrossRef]
6. Barkov, A.Y.; Nixon, G.T.; Levson, V.M.; Martin, R.F.; Fleet, M.E. Chromian spinel from PGE-bearing placer deposits, British Columbia, Canada: Mineralogical associations and provenance. *Can. Mineral.* **2013**, *51*, 501–536. [CrossRef]
7. Zaccarini, F.; Garuti, G.; Pushkarev, E.; Thalhammer, O. Origin of platinum group minerals (PGM) inclusions in chromite deposits of the Urals. *Minerals* **2018**, *8*, 379. [CrossRef]
8. O'Driscoll, B.; VanTongeren, J.A. Layered intrusions: From petrological paradigms to precious metal repositories. *Elements* **2017**, *13*, 383–389. [CrossRef]
9. Irvine, T.N. Origin of chromitite layers in the Muskox intrusion and other stratiform intrusions: A new interpretation. *Geology* **1977**, *5*, 273. [CrossRef]
10. Naldrett, A.J.; Wilson, A.; Kinnaird, J.; Yudovskaya, M.; Chunnett, G. The origin of chromitites and related PGE mineralization in the Bushveld Complex: New mineralogical and petrological constraints. *Miner. Depos.* **2012**, *47*, 209–232. [CrossRef]
11. Barnes, S.J.; Roeder, P. The range of spinel compositions in terrestrial mafic and ultramafic rocks. *J. Petrol.* **2001**, *42*, 2279–2302. [CrossRef]
12. Johan, Z.; Martin, R.F.; Ettler, V. Fluids are bound to be involved in the formation of ophiolitic chromite deposits. *Eur. J. Mineral.* **2017**, *29*, 543–555. [CrossRef]
13. Murashov, D.F. Ultrabasic intrusions of the Serpentinite Belt (Pados-Tundra etc.). In *Geology of the USSR, Murmanskaya Oblast, Geological Description*; Gosgeoltekhizdat Publisher: Moscow, Russia, 1958; Volume 27, pp. 318–321. (In Russian)
14. Vinogradov, L.A. Formations of Alpine-type ultrabasic rocks in the southwestern part of the Kola Peninsula (The Notozerskiy ultrabasic belt). In *Problems of Magmatism of the Baltic Shield*; Nauka Publisher: Leningrad, Russia, 1971; pp. 147–153. (In Russian)

15. Mamontov, V.P.; Dokuchaeva, V.S. The geology and ore potential of the Pados-Tundra massif in the Kola Peninsula. *Otech. Geol.* **2005**, *6*, 52–60. (In Russian)

16. Barkov, A.Y.; Nikiforov, A.A.; Martin, R.F. The structure and cryptic layering of the Pados-Tundra ultramafic complex, Serpentinite Belt, Kola Peninsula, Russia. *Bull. Geol. Soc. Finl.* **2017**, *89*, 35–56. [CrossRef]

17. Barkov, A.Y.; Nikiforov, A.A.; Tolstykh, N.D.; Shvedov, G.I.; Korolyuk, V.N. Compounds of Ru–Se–S, alloys of Os–Ir, framboidal Ru nanophases, and laurite–clinochlore intergrowths in the Pados-Tundra complex, Kola Peninsula, Russia. *Eur. J. Mineral.* **2017**, *29*, 613–621. [CrossRef]

18. Barkov, A.Y.; Nikiforov, A.A.; Halkoaho, T.A.A.; Konnunaho, J.P. The origin of spheroidal patterns of weathering in the Pados-Tundra mafic-ultramafic complex, Kola Peninsula, Russia. *Bull. Geol. Soc. Finl.* **2016**, *88*, 105–113. [CrossRef]

19. Barkov, A.Y.; Nikiforov, A.A.; Korolyuk, V.N.; Barkova, L.P.; Martin, R.F. Anomalous chromite-ilmenite parageneses in the Chapesvara and Lyavaraka ultramafic complexes, Kola Peninsula, Russia. *Period. Mineral.* **2020**, *89*, 299–317.

20. Barkov, A.Y.; Korolyuk, V.N.; Barkova, L.P.; Martin, R.F. Double-front crystallization in the Chapesvara ultramafic subvolcanic complex, Serpentinite Belt, Kola Peninsula, Russia. *Minerals* **2019**, *10*, 14. [CrossRef]

21. Serov, P.A.; Bayanova, T.B.; Steshenko, E.N.; Kunakkuzin, E.L.; Borisenko, E.S. Metallogenic setting and evolution of the Pados-Tundra Cr-Bearing ultramafic complex, Kola Peninsula: Evidence from Sm–Nd and U–Pb isotopes. *Minerals* **2020**, *10*, 186. [CrossRef]

22. Barkov, A.Y.; Nikiforov, A.A.; Barkova, L.P.; Korolyuk, V.N. Komatiitic subvolcanic rocks in the mount Khanlauta massif, Serpentinite Belt, Kola Peninsula. *Russ. Geol. Geophys.* **2021**, in press.

23. Vaasjoki, M. (Ed.) *Radiometric Age Determinations from Finnish Lapland and Their Bearing on the Timing of Precambrian Volcano-Sedimentary Sequences*; Geological Survey of Finland: Espoo, Finland, 2001; Volume 33, p. 279.

24. Balagansky, V.V.; Gorbunov, I.A.; Mudruk, S.V. Palaeoproterozoic Lapland-Kola and Svecofennian Orogens (Baltic Shield). *Her. (Vestn.) Kola Sci. Cent. RAS* **2016**, *3*, 5–11. (In Russian)

25. Nikolaeva, I.V.; Palesskii, S.V.; Koz'menko, O.A.; Anoshin, G.N. Analysis of geologic reference materials for REE and HFSE by inductively coupled plasma-mass spectrometry (ICP-MS). *Geochem. Int.* **2008**, *46*, 1016–1022. [CrossRef]

26. Nikolaeva, I.V.; Palesskii, S.V.; Chirko, O.S.; Chernonozhkin, S.M. Determination of major and trace elements by inductively coupled mass-spectrometry in silicate rocks after fusion with $LiBO_2$. *Anal. Kontrol* **2012**, *8*, 134–142.

27. Karmanova, N.G.; Karmanov, N.S. A universal methodology of X-ray fluorescence analysis of rocks using an ARL-9900XP spectrometer. In Proceedings of the VII All-Russian Conference on X-ray Spectral Analysis, Novosibirsk, Russia, 19–23 September 2011; p. 126. (In Russian).

28. Korolyuk, V.N.; Usova, L.V.; Nigmatulina, E.N. Accuracy in the determination of the compositions of main rock-forming silicates and oxides on a JXA-8100 microanalyzer. *J. Anal. Chem.* **2009**, *64*, 1042–1046. [CrossRef]

29. Lavrent'ev, Y.G.; Korolyuk, V.N.; Usova, L.V.; Nigmatulina, E.N. Electron probe microanalysis of rock-forming minerals with a JXA-8100 electron probe microanalyzer. *Russ. Geol. Geophys.* **2015**, *56*, 1428–1436. [CrossRef]

30. Barkov, A.Y.; Nikiforov, A.A.; Martin, R.F. A novel mechanism of spheroidal weathering: A case study from the Monchepluton layered complex, Kola Peninsula, Russia. *Bull. Geol. Soc. Finl.* **2015**, *87*, 79–85. [CrossRef]

31. McDonough, W.F.; Sun, S.-S. The composition of the Earth. *Chem. Geol.* **1995**, *120*, 223–253. [CrossRef]

32. Craig, J.R.; Scott, S.D. Sulfide phase equilibria. In *Sulfide Mineralogy*; Ribbe, P.H., Ed.; Reviews in Mineralogy, Mineral; Walter de Gruyter GmbH & Co. KG: Washington, DC, USA, 1974; Volume 1, pp. CS1–CS110.

33. Jamieson, H.E.; Roeder, P.L. The distribution of Mg and Fe^{2+} between olivine and spinel at 1300 °C. *Am. Mineral.* **1984**, *69*, 283–291.

34. Balagansky, V.V.; Glebovitsky, V.A. The Lapland Granulite Belt and the Tanaelv Belt. In *Early Precambrian of the Baltic Shield*; Nauka: Saint-Petersburg, Russia, 2005; pp. 127–175. (In Russian)

35. Leont'eva, O.P.; Belonin, M.D. *Geological Map of Mineral Resources of the USSR (Scale 1:200,000; Q-35-VI)*; Shurkin, K.A., Ed.; Kola Series; Northwestern Geological Department, Ministry of Geology and Mineral Resource Protection of the USSR, Gosgeoltekhizdat: Moscow, Russia, 1964.

36. Barkov, A.Y.; Martin, R.F.; Izokh, A.E.; Nikiforov, A.A.; Korolyuk, V.N. Ultramagnesian olivine in the layered complexes Monchepluton (Fo_{96}) and Pados-Tundra (Fo_{93}), Kola Peninsula. *Russ. Geol. Geophys.* **2021**, in press. [CrossRef]

37. Puchtel, I.S.; Haase, K.M.; Hofmann, A.W.; Chauvel, C.; Kulikov, V.S.; Garbe-Schönberg, C.-D.; Nemchin, A.A. Petrology and geochemistry of crustally contaminated komatiitic basalts from the Vetreny Belt, southeastern Baltic Shield: Evidence for an early Proterozoic mantle plume beneath rifted Archean continental lithosphere. *Geochim. Cosmochim. Acta* **1997**, *61*, 1205–1222. [CrossRef]

38. Kulikov, V.S. Highly magnesian volcanism in the Early Proterozoic time. In *Komatiites and Highly Magnesian Volcanic Rocks of the Early Precambrian in the Baltic Shield*; Bogatikov, O.A., Ed.; Nauka Press: Leningrad, Russia, 1988; pp. 20–88. (In Russian)

39. Kulikov, V.S.; Bychkova, Y.V.; Kulikova, V.V. The Vetreny belt: An Early Proterozoic tectonic and petrologic type of the southeastern Fennoscandia. In *Geology of Karelia from the Archean Time to the Present, Proceedings of the All-Russian Conference Devoted to the 50th Anniversary of the Institute of Geology, Petrozavodsk, Russia, 24–26 May 2011*; Institute of Geology, KarRC, RAS: Petrozavodsk, Russia, 2011; pp. 91–103. (In Russian)

40. Sharkov, E.V.; Bogatikov, O.A.; Grokhovskaya, T.L.; Chistyakov, A.V.; Ganin, V.A.; Grinevich, N.G.; Snyder, G.A.; Taylor, L.A. Petrology and Ni–Cu–Cr–PGE mineralization of the largest mafic pluton in Europe: The Early Proterozoic Burakovsky layered intrusion, Karelia, Russia. *Int. Geol. Rev.* **1995**, *37*, 509–525. [CrossRef]

41. Chistyakov, A.V.; Sharkov, E.V. Petrology of the Early Paleoproterozoic Burakovsky complex, southern Karelia. *Petrology* **2008**, *16*, 63–86. [CrossRef]

42. Hanski, E.; Huhma, H.; Rastas, P.; Kamenetsky, V.S. The Palaeoproterozoic komatiite–picrite association of Finnish Lapland. *J. Petrol.* **2001**, *42*, 855–876. [CrossRef]

43. Smolkin, V.F. *The Komatiitic and Picritic Magmatism of Early Precambrian in the Baltic Shield*; Nauka: Saint Petersburg, Russia, 1992; p. 272. (In Russian)

44. Hanski, E.J.; Smolkin, V.F. Iron- and LREE-enriched mantle source for early Proterozoic intraplate magmatism as exemplified by the Pechenga ferropicrites, Kola Peninsula, Russia. *Lithos* **1995**, *34*, 107–125. [CrossRef]

45. Arndt, N.T. Thick, layered peridotite–gabbro lava flows in Munro Township, Ontario. *Can. J. Earth Sci.* **1977**, *14*, 2620–2637. [CrossRef]

46. Arndt, N.T. Differentiation of komatiite flows. *J. Petrol.* **1986**, *27*, 279–301. [CrossRef]

47. Arndt, N. Komatiites, kimberlites, and boninites. *J. Geophys. Res. Solid Earth* **2003**, *108*. [CrossRef]

48. Nesbitt, R.W.; Sun, S.S.; Purvis, A.C. Komatiites: Geochemistry and genesis. *Can. Mineral.* **1979**, *17*, 165–186.

49. Nesbitt, R.W.; Jahn, B.-M.; Purvis, A.C. Komatiites: An early Precambrian phenomenon. *J. Volcanol. Geotherm. Res.* **1982**, *14*, 31–45. [CrossRef]

50. Sun, S.-S.; Nesbitt, R.W. Petrogenesis of Archaean ultrabasic and basic volcanics: Evidence from rare earth elements. *Contrib. Mineral. Petrol.* **1978**, *65*, 301–325. [CrossRef]

51. Robin-Popieul, C.C.M.; Arndt, N.T.; Chauvel, C.; Byerly, G.R.; Sobolev, A.V.; Wilson, A. A New model for Barberton komatiites: Deep critical melting with high melt retention. *J. Petrol.* **2012**, *53*, 2191–2229. [CrossRef]

52. Rollinson, H. The Archean komatiite-related Inyala chromitite, southern Zimbabwe. *Econ. Geol.* **1997**, *92*, 98–107. [CrossRef]

53. Herzberg, C.; Condie, K.; Korenaga, J. Thermal history of the Earth and its petrological expression. *Earth Planet. Sci. Lett.* **2010**, *292*, 79–88. [CrossRef]

54. Norman, M.D.; Garcia, M.O. Primitive magmas and source characteristics of the Hawaiian plume: Petrology and geochemistry of shield picrites. *Earth Planet. Sci. Lett.* **1999**, *168*, 27–44. [CrossRef]

55. Matzen, A.K.; Baker, M.B.; Beckett, J.R.; Stolper, E.M. Fe–Mg partitioning between olivine and high-magnesian melts and the nature of Hawaiian parental liquids. *J. Petrol.* **2011**, *52*, 1243–1263. [CrossRef]

56. Le Bas, M.J. IUGS reclassification of the high-Mg and picritic volcanic rocks. *J. Petrol.* **2000**, *41*, 1467–1470. [CrossRef]

57. Eales, H.V.; Costin, G. Crustally contaminated komatiite: Primary source of the chromitites and Marginal, Lower, and Critical Zone magmas in a staging chamber beneath the Bushveld Complex. *Econ. Geol.* **2012**, *107*, 645–665. [CrossRef]

58. Yudovskaya, M.A.; Naldrett, A.J.; Woolfe, J.A.S.; Costin, G.; Kinnaird, J.A. Reverse compositional zoning in the Uitkomst chromitites as an indication of crystallization in a magmatic conduit. *J. Petrol.* **2015**, *56*, 2373–2394. [CrossRef]

59. Wilson, A.H. The earliest stages of emplacement of the eastern Bushveld Complex: Development of the Lower Zone, Marginal Zone and Basal Ultramafic Sequence. *J. Petrol.* **2015**, *56*, 347–388. [CrossRef]

60. Chernosky, J.V., Jr. The upper stability of clinochlore at low pressure and the free energy of formation Mg-cordierite. *Am. Mineral.* **1974**, *59*, 496–507.

61. Kullerud, G.; Yund, R.A. The Ni-S system and related minerals. *J. Petrol.* **1962**, *3*, 126–175. [CrossRef]

62. Sugaki, A.; Kitakaze, A. High form of pentlandite and its thermal stability. *Am. Mineral.* **1998**, *83*, 133–140. [CrossRef]

63. Chashchin, V.V.; Galkin, A.S.; Ozeryanskii, V.V.; Dedyukhin, A.H. The Sopcheozyorsky deposit of chromite and its platinum potential, Monchegorsky pluton (Kola Peninsula, Russia). *Geol. Ore Depos.* **1999**, *41*, 507–515. (In Russian)

64. Lavrov, M.M.; Rezhenova, S.A.; Trofimov, N.N. The composition of chromian spinels of the Burakovsky layered intrusion. In *Proceedings on the Metallogeny of Karelia*; Institute of Geology of the Karelian Science Centre of the RAS: Petrozavodsk, Russia, 1987; pp. 138–151. (In Russian)

65. Alapieti, T.T.; Huhtelin, T.A. The Kemi intrusion and associated chromitite deposit. In *Early Palaeoproterozoic (2.5–2.4) Tornio–Näränkävaara Layered Intrusion Belt and Related Chrome and Platinum-Group Element Mineralization, Northern Finland*; Alapieti, T.T., Kärki, A.J., Eds.; Field trip guidebook for the 10-th Platinum Symposium; Geological Survey of Finland: Oulu, Finland, 2005; pp. 13–32, Guide 51a, Chapter 2.

66. Simon, G.; Kesler, S.E.; Essene, E.J. Phase relations among selenides, tellurides, and oxides; II, Applications to selenide-bearing ore deposits. *Econ. Geol.* **1997**, *92*, 468–484. [CrossRef]

67. Dreibus, G.; Palme, H.; Spettel, B.; Zipfel, J.; Wänke, H. Sulfur and selenium in chondritic meteorites. *Meteoritics* **1995**, *30*, 439–445. [CrossRef]

68. Lorand, J.-P.; Alard, O.; Luguet, A.; Keays, R.R. Sulfur and selenium systematics of the subcontinental lithospheric mantle: Inferences from the Massif Central xenolith suite (France). *Geochim. Cosmochim. Acta* **2003**, *67*, 4137–4151. [CrossRef]

69. Holwell, D.A.; Keays, R.R.; McDonald, I.; Williams, M.R. Extreme enrichment of Se, Te, PGE and Au in Cu sulfide microdroplets: Evidence from LA-ICP-MS analysis of sulfides in the Skaergaard Intrusion, east Greenland. *Contrib. Mineral. Petrol.* **2015**, *170*, 5–6. [CrossRef]

70. Smith, J.W.; Holwell, D.A.; McDonald, I.; Boyce, A.J. The application of S isotopes and S/Se ratios in determining ore-forming processes of magmatic Ni–Cu–PGE sulfide deposits: A cautionary case study from the northern Bushveld Complex. *Ore Geol. Rev.* **2016**, *73*, 148–174. [CrossRef]

71. Howard, J.H. Geochemistry of selenium: Formation of ferroselite and selenium behavior in the vicinity of oxidizing sulfide and uranium deposits. *Geochim. Cosmochim. Acta* **1977**, *41*, 1665–1678. [CrossRef]

72. Ewers, G.R. Experimental hot water-rock interactions and their significance to natural hydrothermal systems in New Zealand. *Geochim. Cosmochim. Acta* **1977**, *41*, 143–150. [CrossRef]